Carbon-supported Single Metal Site Catalysts for Electrochemical CO_2 Reduction to CO and Beyond

Yuanzhi Zhu,[1] Xiaoxuan Yang,[1] Cheng Peng, Cameron Priest, Yi Mei, and Gang Wu**

Dr. Y. Zhu, C. Peng, Prof. Y. Mei

Faculty of Chemical Engineering

Yunnan Provincial Key Laboratory of Energy Saving in Phosphorus Chemical Engineering and New Phosphorus Materials

Kunming University of Science and Technology

Kunming 650500, China

E-mail: meiyi412@126.com

X. Yang, C. Priest, Prof. G. Wu

Department of Chemical and Biological Engineering

University at Buffalo

The State University of New York

Buffalo, NY 14260, USA

E-mail: gangwu@buffalo.edu

1 These two authors contributed equally.

The electrochemical CO_2 reduction reaction (CO_2RR) is a promising strategy to achieve electrical-to-chemical energy storage while closing the global carbon cycle. The carbon-supported single-atom catalysts (SACs) have great potential for electrochemical CO_2RR due to their high efficiency and low cost. The metal centers' performance is related to the local coordination environment and the long-range electronic intercalation from the carbon substrates. This review summarizes the

recent progress on the synthesis of carbon-supported SACs and their application towards electrocatalytic CO_2 reduction to CO and other C_1 and C_2 products. Several SACs are involved, including MN_x catalysts, heterogeneous molecular catalysts, and the covalent organic framework (COF) based SACs. The controllable synthesis methods for anchoring single-atom sites on different carbon supports are introduced, focusing on the influence that precursors and synthetic conditions have on the final structure of SACs. For the CO_2RR performance, the intrinsic activity difference of various metal centers and the corresponding activity enhancement strategies *via* the modulation of the metal centers' electronic structure are systematically summarized, which may help promote the rational design of active and selective SACs for CO_2 reduction to CO and beyond.

Keywords: carbon-supported single-atom, electrocatalyst, CO_2 reduction, metal-substrate intercalation.

1. Introduction

Carbon dioxide (CO_2) is one of the most oxidized carbon forms with an extremely stable chemical structure. With the increasingly severe global climate change problem caused by anthropogenic CO_2 emissions, maintaining the global CO_2 balance for economic and socially sustainable development has become an important research topic. The electrochemical reduction of CO_2 (CO_2RR) into value-added fuels and chemicals, driven by renewable electricity sources, is a promising route for closing the carbon cycle and realizing renewable energy conversion and storage.[1] CO_2RR is a thermodynamically uphill process involving a complex multi-electron transfer and several intermediates (Equations 1–6).[2] Thus, highly active electrocatalysts are

needed to speed up reaction kinetics, especially at mild reaction conditions. In the past 30 years, various electrocatalysts have been explored for the CO_2RR, such as the metal compounds and metal-free heteroatom-doped carbon materials.[3] Based on different catalysts and reaction pathways, more than 16 different products have been obtained, such as CO and HCOOH *via* a two-electron process, HCHO *via* a four-electron process, CH_4 *via* an eight-electron process, as well as multi-carbon (C_{2+}) products (*e.g.*, ethylene and ethanol) *via* C–C coupling.[4] The reduction process is further complicated due to the competing hydrogen evolution reaction (HER), which has similar equilibrium potentials in aqueous electrolytes to the CO_2RR (Equation 7). As a result, the synthesis of an ideal catalyst with high selectivity for a specific product except CO is still a significant challenge.

$$CO_2 + 2H^+ + 2e^- \rightarrow CO + H_2O \qquad E^0 = -0.11 \text{ V } \textit{vs.} \text{ RHE} \quad (1)$$

$$CO_2 + 2H^+ + 2e^- \rightarrow HCOOH \qquad E^0 = -0.12 \text{ V } \textit{vs.} \text{ RHE} \quad (2)$$

$$CO_2 + 6H^+ + 6e^- \rightarrow CH_3OH + H_2O \qquad E^0 = +0.03 \text{ V } \textit{vs.} \text{ RHE} \quad (3)$$

$$CO_2 + 8H^+ + 8e^- \rightarrow CH_4 + 2H_2O \qquad E^0 = +0.17 \text{ V } \textit{vs.} \text{ RHE} \quad (4)$$

$$2CO_2 + 12H^+ + 12e^- \rightarrow C_2H_4 + 4H_2O \qquad E^0 = +0.07 \text{ V } \textit{vs.} \text{ RHE} \quad (5)$$

$$2CO_2 + 12H^+ + 12e^- \rightarrow C_2H_5OH + 3H_2O \qquad E^0 = +0.08 \text{ V } \textit{vs.} \text{ RHE} \quad (6)$$

$$2H^+ + 2e^- \rightarrow H_2 \qquad E^0 = 0 \textit{ vs.} \text{ RHE} \quad (7)$$

Recently, single-atom catalysts (SACs) on carbon-supported substrates have been demonstrated as excellent electrocatalysts for a variety of chemical reactions such as oxygen[5] and nitrogen reactions [6] due to their maximum atomic utilization efficiency, unsaturated metal

coordination, and good conductivity.[7] Several optimization strategies have also been developed to improve the CO_2RR performance of SACs, including reducing the coordination number,[8] tuning the coordination atoms,[9] inducing axial ligands,[10] and constructing structural defects in supports.[11] Many Ni, Fe, and Co-based SACs have exhibited high electrocatalytic activity and Faradaic effectivity (FE) for the CO_2RR with CO as the primary product, due to the optimized adsorption energies of *COOH and *CO intermediates, as well as the high activation barrier for the HER. However, SACs still suffer from some disadvantages, such as difficulty in synthesis and characterizations. The high surface energy and reactivity of single atoms leads to aggregation and much work remains to be done.

As mentioned above, the dispersal of single atoms is mostly carried out on carbon materials. Various carbon materials, such as graphene, carbon nanotubes (CNT), graphitic carbon nitride (g-C_3N_4), and covalent organic frameworks (COFs) could serve as an ideal substrate to provide densely dispersed SACs sites with encouraging activity and selectivity, due to their high electrical conductivity, large specific surface area, and diverse chemical structure. Moreover, for atomically dispersed metal centers, their reaction intermediates' adsorption and desorption behaviors are highly dependent on the surrounding coordination environment and the long-range electronic intercalation from the carbon substrates. However, direct conversion of CO_2 into other deeply reduced products are more attractive because they are essential chemical intermediates for many industrial processes. Some pioneering works have reported the formation of HCOOH,[12] methanol (CH_3OH),[13] CH_4,[14] ethanol (C_2H_5OH),[15] and ethane (C_2H_4)[16]. The catalytic mechanisms involve the synergistic effect between metal sites and surrounding heteroatoms,[17] the optimized *CO adsorption energy for new reaction pathways,[13a] the reversible formation of metal clusters,[15] and the densely dispersed SACs sites to trigger the C-C coupling.[16] Although some

excellent reviews have been devoted to applying SACs for the CO_2RR, few of them systematically discussed the conversion of CO_2 into products beyond CO.

In this review, we first give some fundamentals for carbon-supported SACs in CO_2RR, including primary classification of SACs and the theoretical basis to form CO and other products on SACs sites. Then, the typical preparation methods for carbon-supported SACs with CO_2RR activity are summarized, emphasizing tuning the coordination structure of SACs through rational control of experimental conditions. Finally, the applications of carbon-based SACs in electrochemical CO_2 reduction to CO and beyond are discussed. We mainly focus on the difference in the intrinsic activity of various metal centers and summarize the corresponding activity enhancement strategies *via* the modulation of the metal centers' electronic structure, which may help promote the rational design of active and selective SACs for the CO_2RR.

2. Classification of Carbon-supported SACs for the CO_2RR

Several types of carbon-supported SACs, including the MN_x catalysts, the heterogeneous molecular catalysts, and COFs based SACs, have received growing interest and shown their unique advantages for electrochemical CO_2RR, which are classified and briefly introduced in the following section.

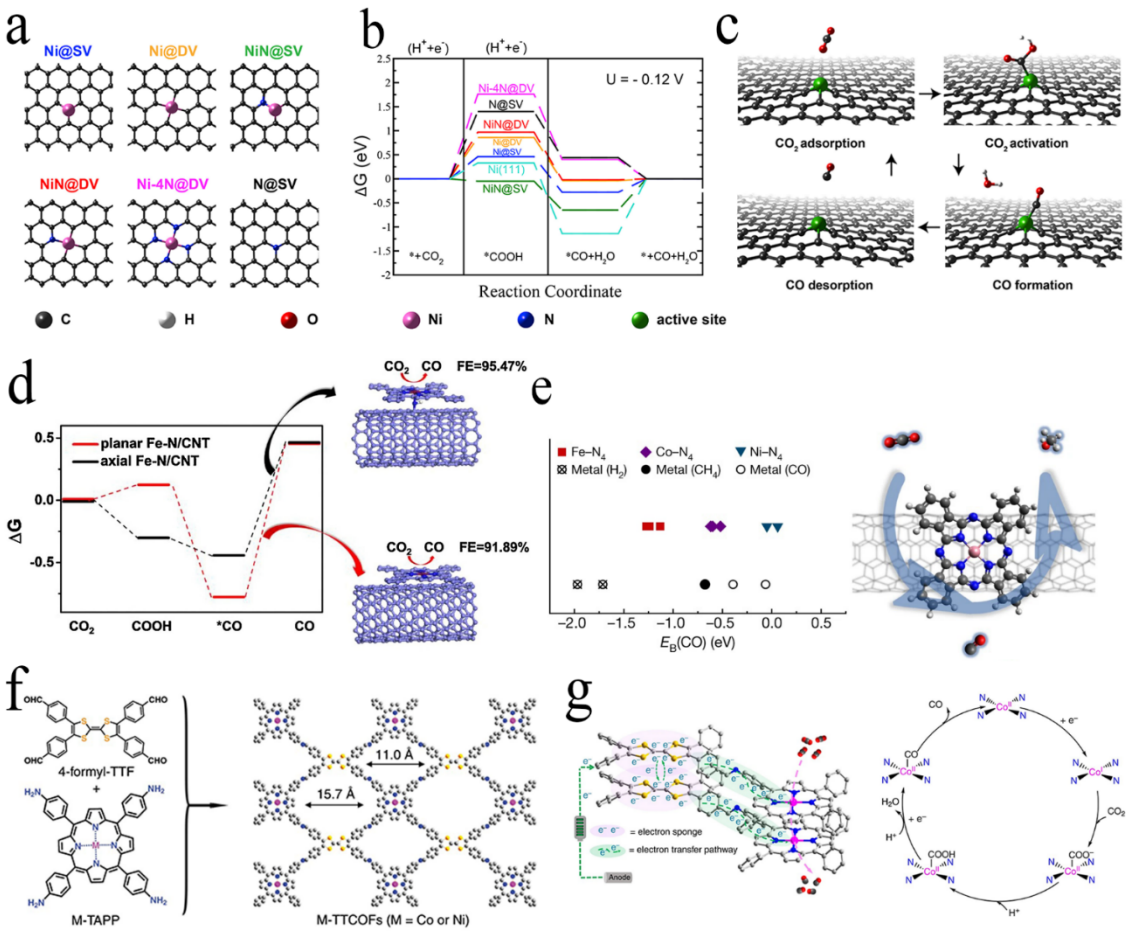

Figure 1. The typical structures for different types of CO_2RR active SACs. (a) The schematic illustration of metal atoms coordinated by N or C atoms in graphene to form MN_xC_y sites, (b) corresponding CO_2RR free energy diagram, and (c) reaction pathway for CO production. Reproduced with permission.[18] Copyright 2017, Elsevier. (d) The schematic illustration of the molecule catalyst (FeTPP) is immobilized on CNT *via* axial coordination or noncovalent intercalation and the comparison of adsorption energy for intermediates. Reproduced with permission.[19] Copyright 2020, Elsevier. (e) The molecular catalyst with a well-defined structure immobilized on carbon support by noncovalent intercalation and computed CO binding energies. Reproduced with permission.[13a] Copyright 2019, Nature Publishing Group. (f) The formation of

COFs as a building block and (g) proposed a schematic mechanism for the electrocatalytic CO_2RR on it. Reproduced with permission.[20] Copyright 2020, Nature Publishing Group.

2.1 Isolated Metal Atoms Embedded into Carbon-based Skeleton

MN_xC_y (M = Ni, Fe, Co, *etc*.) catalysts (**Figure 1a–c**) are the most widely studied carbon-supported SACs for the CO_2RR.[18] During the past decade, tremendous research has focused on developing modified MN_xC_y for catalyzing the CO_2RR. Some useful methods, including many types of defects or heteroatoms on carbon substrates *e.g.*, vacancy defects,[21] edge,[22] pyridine-type N,[23] and pyrrole-type N[9, 24], have been reported as useful anchor sites to stabilize various single atoms.

The carbon structure's diversity plays a significant role in modulating the electronic structure of the metal centers, leading to unusual scaling relationships, new reaction mechanisms, and tunable catalytic selectivity. As the synthesis usually involves high-temperature pyrolysis of complex precursors, MN_xC_y catalysts commonly possess short-range order but long-range disorder in structure, even if derived from crystalline carbon precursors, *e.g.*, graphene, carbon nanotubes, and metal-organic frameworks (MOFs), *etc*. As a result, some MN_xC_y sites with relatively low theoretical activity and selectivity have been demonstrated effective for the CO_2RR, with such effectiveness attributed to the change in the local coordination environment. For example, intact CoN_4 sites on graphene are more favorable for the HER due to its suitable H* adsorption and CO* binding strong enough to inhibit the desorption. However, decreasing the N coordination or constructing edge-host CoN_{2+2} sites could improve the CO_2RR selectivity for CO production, attributed to the optimization in CO_2* adsorption and COOH dissociation.[8, 22a, 25] Some Ni-based

SACs without significant differences in structure have also exhibited high activity and selectivity for either CO_2RR or HER.[24b, 26] However, owing to the lack of precisely controllable synthesis methods, the switching behavior in catalytic selectivity of MN_xC_y is still elusive. It is still a significant challenge to realize the rational design of MN_xC_y materials in the experiment.

2.2 Molecular Catalyst Supported on Conductive Carbon Substrates

Some metal complexes composed of metal centers and macrocyclic chelating ligands, such as metal porphyrins and metal phthalocyanines, have been demonstrated effective for electrocatalytic CO_2RR.[27] They possess a well-defined active center, and the coordination environment could be easily controlled by tuning the ligand structure. Immobilizing these molecular catalysts onto conductive substrates can effectively enhance the conductivity and prevent molecular aggregation, leading to enhanced stability and atomic utilization. The molecular catalysts could be covalently[28]/non-covalently[13a, 29] absorbed on the substrates (**Figure 1e**), or anchored by axial coordination intercalation between the metal centers and the heteroatoms on substrates (**Figure 1d**).[19] Most immobilization conditions only involve simple liquid mixing of the precursors with a gentle heating treatment, which guarantees high structure correlation between the metal complexes and the derived heterogeneous catalysts. Unlike MN_xC_y catalysts that often comprise complex coordination environments, the heterogeneous molecular catalysts have apparent advantages due to their uniform and well-defined structures, facilitating the understanding of the CO2RR mechanism at the molecular level.

Similarly, the carbon substrate's unique intercalation also plays a significant role in tuning the adsorption energy of the intermediates on metal centers. In some cases, both the specific macrocyclic ligands and the substrate are indispensable in realizing the multi-electron reduction

of CO_2 to products other than CO. For example, the 6-electron reduction of CO_2 to methanol can proceed on CNT-supported Co phthalocyanine with a remarkable FE of over 40%.[13a] The selectivity decreased significantly when phthalocyanine was replaced by chlorine or porphyrin, or when the CNT was replaced by carbon fiber paper or conductive carbon black.

For simple electrochemical reactions involving only a few intermediates that convert to a single product (*e.g.*, HER and OER), more attention is paid to pursuing a well-developed porous structure and high conductivity in order to mitigate the diffusion limit and obtain large current density under high overpotential. However, the selectivity of CO_2RR is closely related to the competing HER process. The relative rate between CO_2RR and HER not only depends on the intrinsic selectivity of active sites but also on the local concentration of the rate-determining intermediates for each reaction, which is related to more complicated mesostructures (*e.g.*, roughness) of the electrocatalyst besides specific surface area.[31] As many heterogeneous molecular catalysts are physically maintained through non-covalent forces, their mass transfer behavior could be easily tuned by changing the substrate with different mesostructures. Wang *et al*. reported the synthesis of two heterogeneous molecular catalysts with phen-Cu complexes supported on graphene or graphene oxide (GO) by simple liquid mixing of $CuCl_2$, 1,10-phen, and carbon substrates.[32] Differing from the GO with nonporous structure, the mesostructure of the graphene matrix favored CO_2 reduction on the Cu center over hydrogen evolution by limiting mass transport from the bulk solution to the electrode surface, leading to much higher selectivity for the CO_2RR. This could be explained by the amplified proton depletion effects on a porous electrode and the fact that the HER was strongly dependent on the proton donor environment while the CO_2RR was not.

As molecular catalysts with conjugated structure tend to stack and aggregate *via* intermolecular metal−nitrogen bonding, the noncovalent immobilization method can hardly achieve the theoretical monolayer coverage on carbonaceous substrates, resulting in relatively low SACs loading.[33] The non-covalently immobilized catalysts may also suffer from a leaching issue during long-term operation. One solution is to directly graft molecular catalysts onto the conductive substrates *via* covalent bonding. Co and Fe-based porphyrin complexes have been covalently linked to diamond and CNT *via* the azide-alkyne cycloaddition,[34] and C–C coupling reaction.[30] Co porphyrin has also been anchored on the carbon substrates by axial coordination intercalation based on liquid-phase reactions.[28] In particular, under the catalysis of triethanolamine, the cobalt (III) protoporphyrin IX chloride (CoPPCl) can react with hydroxyl-functionalized CNT (CNT-OH) to form heterogeneous Co porphyrin catalyst *via* the breaking of the Co–Cl bond and the formation of the Co–O bond. This covalently grafted catalyst exhibited improved Co SACs dispersion and higher CO2RR activity and long-term stability compared against the physically mixed control sample. This higher performance can be attributed to the strong catalyst–substrate intercalation through the Co–O covalent bond.

2.3 Metal Sites in Covalent Organic Frameworks

Fabricating COFs with active metal sites as building blocks is another effective strategy to improve the electrocatalytic activity and stability for the CO_2RR (**Figure 1f–g**).[20, 35] COFs are an emerging porous material synthesized by crosslinking rigid aromatic molecules based on reversible covalent bonds, possessing extended π-conjugation structure, tunable composition, and sufficient porosity. This class of materials bridges the gap between heterogeneous and homogeneous electrocatalysts by inheriting small molecules' activity and selectivity while

simultaneously improving the conductivity and mass transfer efficiency due to the π-conjugation structure and developed porosity. Many metal porphyrins and phthalocyanines have been used as the building blocks of COFs for electrochemical reduction of CO_2 to CO, including Co, Ni, Fe-based porphyrins, and phthalocyanines.[36] The CO_2RR performance of COFs-based SACs is positively related to the COFs framework. For instance, Lin *et al*.[35a] synthesized a Co porphyrin-based COF by condensation reaction between 4-aminophenyl modified Co-porphyrin and 1,4-benzenedicarboxaldehyde (BDA), which exhibited much-improved activity for CO_2 reduction to CO with negligible degradation over 24 hours. Replacing BDA with 4,4'-dicarboxaldehyde (BPDA) could increase the pore size and specific surface area for the derived COFs, affording 2.2-fold enhancement in current density at –0.67 V, attributed to the increased number of accessible Co SACs sites. Additionally, the in-situ X-ray absorption spectroscopy (XAS) analysis observed partial reduction of Co (II) to Co (I) during the CO_2RR process, which indicates the electronic structure of Co centers could be further modulated after the formation of π-conjugation network structure.

The atomically dispersed metal sites can also be anchored into heteroatom-containing COFs to form CO_2RR active SACs. The covalent triazine frameworks (CTFs) with rich pyridine-like N anchor sites have been directly utilized as a substrate for Co and Ni-based SACs, showing good activity and selectivity reduction of CO_2 to CO and C_2H_4.[37] Compared with the MN_xC_y catalysts from high-temperature synthesis, the well-defined structures of COFs provide more precise information for the identification of active sites and corresponding catalytic mechanism. In this sense, some 2D crystalline materials could also be ideal candidates for the immobilization of SACs. For instance, the SACs sites (*e.g.*, Cu and Ag) on g-C_3N_4 have been demonstrated to be useful for the CO_2RR to produce CO and some other C_1 or C_2 products.[17, 38] Graphdiyne (GDY) has been

predicted as an ideal candidate for anchoring metal atoms to produce multi-electron CO_2 reduction products like CH_4 and ethanol.[39]

3. Synthesis of SACs on Carbon-supported Substrates

According to theoretical and experimental evidence, the electrocatalytic performance of carbon-based SACs is positively related to the population of active sites, the configuration of the metal centers, and the size and porosity of the substrate. However, precisely controllable synthetic methods for SACs remain out of reach. Thanks to advanced characterization technologies, such as scanning transmission electron microscopy (STEM) and X-ray absorption spectroscopy (XAS) analysis, different kinds of SAC configurations have been identified. This supports the establishment of a structure-activity relationship between the local coordination environment and the activity of SACs. However, how the precursors and the reaction conditions influence the final structure of SACs is still elusive, especially for the MN_xC_y materials obtained from the uncontrolled carbonization process. Some works have recently shed some light on the formation process and mechanism of carbon-supported SACs, which give some guidelines for the control synthesis of SACs for the CO_2RR. In this section's discussion, we aim to summarize the recent advances in the controllable synthesis of SACs for application in CO_2RR to give a deep insight into the influence of synthetic conditions on the final structure of SACs and the mechanism involved.

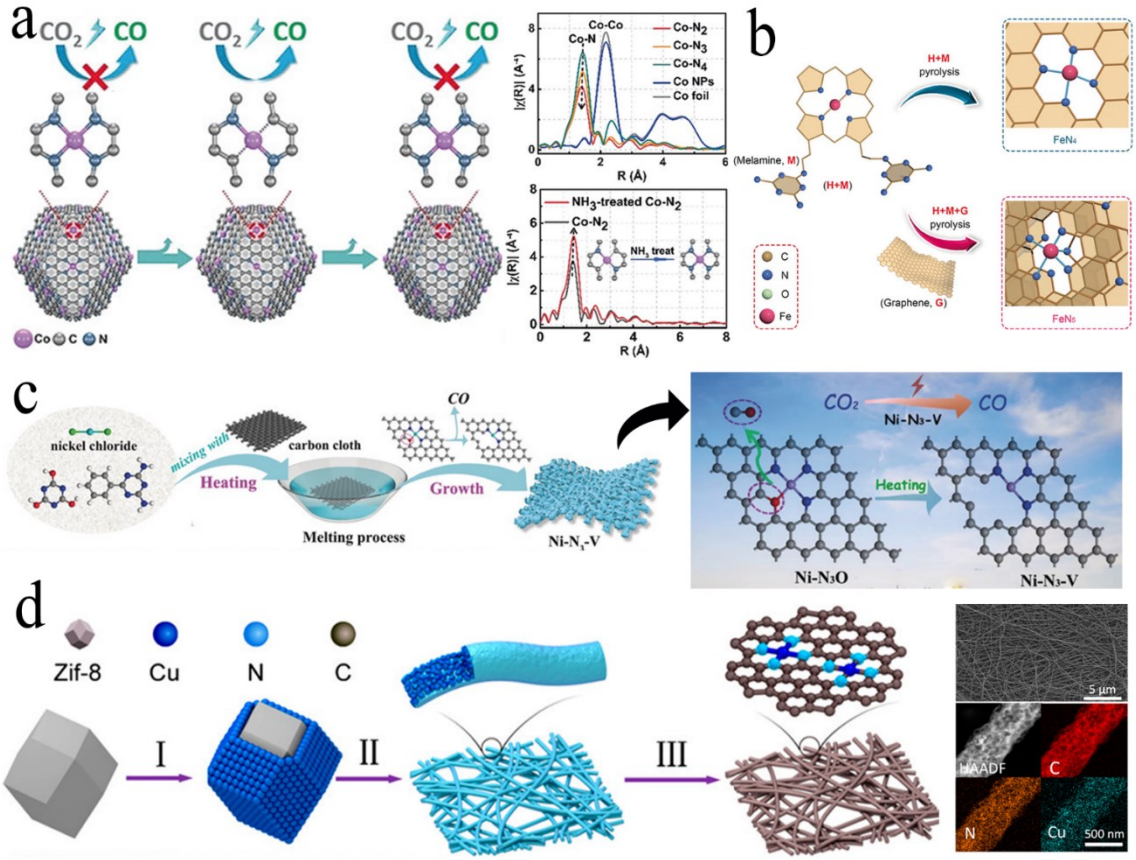

Figure 2. Controllable synthesis of SACs on a carbon-based substrate with various configuration and morphology. (a) The schematic illustration of switching the N coordination number between 4 to 2 *via* a pyrolytic temperature and atmosphere control. Reproduced with permission.[8] Copyright 2017, Wiley-VCH. (b) Synthesis of FeN_5 catalysts by pyrolysis of hemin (H) and melamine (M) co-adsorbed on graphene. Reproduced with permission.[10] Copyright 2019, Wiley-VCH. (c) The schematic illustration for the formation of vacancy defect on the carbon substrates uses O, N-containing precursors. Reproduced with permission.[11] Copyright 2019, Wiley-VCH. (d) Synthesis of CuN_4 on self-standing carbon substrate by electrospinning of precursor followed by carbonization. Reproduced with permission.[13b] Copyright 2019, American Chemical Society.

3.1 Rational Design of Precursors

Pyrolysis of N, C, and metal-containing precursors is an effective method to synthesize carbon-supported SACs with MN_xC_y moieties. MOFs are a class of well-defined coordination polymers composed of various metal ions and organic ligands, featuring tunable morphology, components, and porosity at the molecular level. Zn-based zeolitic imidazolate frameworks (ZIF-8) modified with another transition metal have been extensively demonstrated as ideal precursors for synthesizing MN_xC_y catalysts with considerable CO_2RR activity. MN_xC_y catalysts (M = Ni, Fe, Co, Cu, and Zn, *etc*.) have been obtained by pyrolysis of ZIF-derived precursors for the CO_2RR in recent literature. The target metal resource could be anchored on the node,[8, 21] adsorbed onto the ligand,[40] or confined within MOFs' cavities.[41] During pyrolysis, the evaporation of Zn can create a highly porous structure, and the imidazolate ligands can act as N and C resources to stabilize the nonvolatile target metal atom, which enables the formation of ordered carbonized derivatives with uniformly dispersed SAC sites. As opposed to a random mixing of the N, C, and metal components, various metal atoms could be anchored at the node of the same ZIF-8 skeleton at relatively fixed distances, and the metal agglomeration can be mitigated by Zn volatilization during pyrolysis. This facilitates the control over the metal atom distribution to form dual-metal MN_xC_y with two different metal sites adjacent to the same substrate. By pyrolysis of modified ZIF-8, the Ni-Fe[42] and Fe-Cu[43] dual-metal sites have been synthesized to enhance CO2RR performance synergistically. The ZIF-8 precursors with particle sizes from 50 to 400 nm were prepared by regulating the molar ratio of Zn^{2+} and 2-methylimidazole to investigate the particle size's influence on the CO_2RR activity and selectivity.[44] The ferrocene (Fe resource) was located separately from the ZIF-8 (N, C resource), which was volatilized during heating treatment and trapped by the carbonated ZIF-8 skeleton to form the final sample. The experimental results revealed that particle

size change has no noticeable effect on BET specific surface area, pore size distribution, and element content. However, the CO_2RR performance was found to follow a volcano-like function with respect to particle size. The FeN_x on carbon substrate with a particle size of ~100 nm exhibited the highest CO partial current and FE, which should be attributed to the increased electrochemical surface area through size modulation. In addition to bulk ZIF-8 with rhombododecahedral morphology, the 2D Ni-Zn bimetallic ZIF has also been used as a precursor to synthesize ultrathin 2D carbon substrates with highly exposed NiN_x sites for the CO_2RR.[45]

The difference in synthetic conditions can lead to a different morphology, structure, and atomic density of MN_xC_y. For example, many Co, Fe, and Ni-based MN_x have been obtained from the mixture of GO and metal ions with pentaethylenehexamine,[46] and NH_3[47] as N resource. When replacing the GO with CNT[48] and conductive carbon black, various MN_x (*e.g.*, Co, Fe, and Ni) on corresponding carbon substrates could be formed, which also exhibited high SACs loading and CO_2RR activity for CO production. The g-C_3N_4 is another π-conjugated precursor to prepare MN_x materials, producing exclusive active sites with high activity and selectivity for electrocatalytic CO_2 conversion to CO.[23] Using a multistep pyrolysis process with dicyandiamide[49] or melamine[50] as a precursor, the in-situ formation of g-C_3N_4 can prevent the metal ions from aggregating, thus achieving atomically dispersed MN_x sites with high loading.

3. 2 Engineering the Coordination Environment

Regulating the local environment of metal sites is regarded as an efficient way to optimize the electronic structure of SACs in order to trigger more extraordinary electrochemical CO_2RR performance. Pyrolytic temperature is a crucial factor in regulating the type and number of coordinated N atoms for MN_xC_y. This provides a different local coordination environment for

metal atoms, leading to optimized adsorption energy of intermediates and improved CO_2RR performance. Specifically, pyrolysis of MOF-based precursors under relatively low temperatures (*e.g.*, 700 ºC) predominantly produces intact MN_4 configurations. In contrast, the elevated pyrolytic temperature can cause the loss of coordinated N atoms to form highly CO_2RR active MN_2C_2 configurations (**Figure 2a**).[8] The CoN_2C_2 configuration was also found to reconstitute into a CoN_4 configuration after annealing under NH_3 atmosphere at 400 ºC, ultimately leading to a decrease in CO_2RR activity. Unlike most works using the N-containing ZIF-MOF as a precursor, Gong *et al*. reported the synthesis of a series of NiN_x SACs by pyrolysis of N-free bimetallic MgNiMOF-74 with polypyrrole (PPy) filled into its 1D channels.[51] The introduction of Mg^{2+} in MgNiMOF-74 extends the distance between adjacent Ni atoms, and the PPy can serve as an N resource to stabilize the isolated Ni atoms during pyrolysis. By controlling the pyrolytic temperature, the NiN_4, NiN_3C, and NiN_2C_2 sites could be fabricated at 600, 800, and 900 ºC, respectively. It seems that the relationship between pyrolytic temperature and the N coordination number above is a general tendency, which has also been observed for Fe[44] and Cu[52] based samples. However, some works also reported that higher thermal activation temperature (*e.g.*, 1000 ºC) could promote MN_4 sites' synthesis, [53] thus producing more graphitic N in the carbonaceous frameworks induces charge redistribution and enhance electron-transport properties.[44] Other reaction factors, such as pyrolytic time and thermal stability of the precursor, may also influence the configuration of MN_x sites.

In general, only MN_x with an N coordination number less than four can be obtained through conventional pyrolysis methods. Zhang *et al*. reported the synthesis of atomically dispersed FeN_5 active sites supported on N doped graphene for efficient CO_2RR.[10] The FeN_5 SACs were synthesized by thermal pyrolysis of hemin (H) and melamine (M) co-adsorbed on graphene (G).

The cross-linking of H and M at elevated temperatures suppresses the aggregation of iron atoms and provides a rich nitrogen source to introduce the N-dopant into graphene and anchors an individual iron atom for the formation of a unique FeN_5 active site (**Figure 2b**). The axial pyrrolic N ligand of the FeN_5 site further depletes the electron density of Fe 3d orbitals. It reduces the Fe–CO π back-donation, thus enabling the rapid desorption of CO and high selectivity towards CO production.

In addition to the N coordination number, the type of coordinated N atoms (*e.g.*, pyridinic N or pyrrolic N) also plays an essential role in tuning the electronic structure and CO_2RR activity of the metal center.[48] The work by Gu *et al*. revealed that the MN_xC_y materials are more likely to inherit the original pyridinic or pyrrolic N atoms in the precursors.[9] To be specific, pyrolysis of Fe-modified ZIF-8 with imidazole ligands under 800 ºC can produce a stable +3 oxidation state of Fe center with pyrrolic-type N configuration, giving rise to easier CO* desorption for improved CO production. Whereas pyrolysis of Fe-phenanthroline complex at 700 ºC mainly produces pyridinic-type FeN_4 sites, in which the Fe^{3+} centers are quickly reduced to Fe^{2+} with low CO_2RR activity at high overpotentials. The temperature may also have some effect on the type of N atoms during the pyrolytic process. In another case, with glucose, dicyandiamide and iron (III) chloride as precursors, the ratio of pyrrolic to pyridinic N in FeN_x catalyst increased with the increase in pyrolytic temperature from 800 to 1000 ºC, accompanied by improved CO_2RR performance.[24a]

The reduction of CO_2 to COOH* is generally regarded as the rate-limiting step for the CO_2RR on MN_x based electrocatalysts. The introduction of vacancy defects within the catalysts could improve the binding and activation of CO_2 reactants on electrocatalysts. In particular, the DFT calculations revealed that the vacancy defect at the MN_x sites (M = Ni or Cu) could enhance the

absorption energies of *COOH and weaken the CO* binding energy on MN_x sites, facilitating CO formation and inhibiting the competing H* adsorption for the HER.[21] Good selection of the precursor and increasing the pyrolytic temperature are effective strategies to create an unsaturated coordination environment in MN_x. Zheng *et al*. reported the synthesis of undercoordinated CuN_2 sites on the graphene matrix by pyrolysis of the mixture of graphene, chlorophyllin, and dicyandiamide at 900 °C.[52] Decreasing the pyrolytic temperature to 700-800 °C could predominately form the four-coordinated CuN_4 sites. Rong *et al*. synthesized a vacancy defect NiN_3 on carbon cloth by using cyanuric acid (CA), 2,4-diamino-6-phenyl-1,3,5-triazine (DPT), and Ni as a precursor (**Figure 2c**).[11] They suggested that the oxygen-containing precursor plays a vital role in forming a vacancy defect at MN_x sites. During the pyrolytic process, the precursors containing both nitrogen and oxygen atoms can generate an N/O mixing coordinated $Ni\text{-}N_3O$ configuration under 500 °C. The oxygen atom can be removed under-evaluated temperature due to the weaker Ni-O interaction, resulting in a vacancy-defect NiN_3 SACs. For comparison, Ni's reaction with O-free precursor was carried out, and only a no-vacancy-defect $Ni\text{-}N_4$ SAC was obtained. It should be noted that the formation of Ni-O coordination is reasonable, which has been proposed by in-situ XAS in other work.[54]

3. 3 Control the Morphology of Carbon Substrates

Some works have been devoted to the morphology and structure control of the carbon substrates to prepared SACs with a hierarchical pore structure. Incorporating sacrifice templates into the precursors is a common strategy to increase the specific surface area and porosity. Many kinds of templates have been used, including silica nanoparticles,[55] MgO,[56] SBA-15[57], Fe_2O_3 particles,[58] and nano rod-like ZnO.[59] The metal particles formed from excessive metal precursors

during pyrolysis can also act as the rigid templates, which usually introduces mesopores in carbon substrates after being removed by acid washing treatment. In a different case, the specific content of Fe ions within MOFs precursor not only results in densely dispersed FeN_x sites, but also triggers the Kirkendall effect by accelerating decomposition of metal-imidazolate linkages during pyrolysis, thus leading to large mesopores inside the derived carbon substrates.[60] Zhang *et al*[61] reported the synthesis of BiN_4 on porous carbon networks by pyrolysis of bismuth-based MOFs and dicyandiamide. The in-situ TEM analysis revealed the Bi metal first agglomerated into nanoparticles during the heating process, which further transformed into atomic BiN_4 sites with the assistance of NH_3 released from the decomposition of dicyandiamide, leaving a large number of pores on the carbon substrate.

For high-performance electrocatalyst, both efficient mass and electronic transfer are essential features. As critical as porosity to high mass transfer, the 3D cross-linked carbon network plays a crucial role in improving the electron transport efficiency. Some SACs on a composite structure composed of 2D graphene and 1D CNT have been synthesized for electrocatalysis.[62] Pan *et al.* reported FeN4 sites' synthesis on carbon frameworks with graphene nanoribbon attached to the fibrous CNT, achieving high electrochemically active surface area and smooth mass transport.[63] This carbon structure was synthesized through controllable partial unzipping of CNT using $KMNO_4/H_2SO_4$ as oxidants. In contrast, the Fe residues in CNTs synthesized by chemical vapor deposition (CVD) method can be directly used as a Fe source to grow FeN_4 sites.

Many carbon-supported SACs are produced in powder form and need to be coated onto collectors with binders for practical applications. During the binding procedure, the single-atom sites might be blocked by the polymer binders and lose the catalytic activity in CO_2RR. Therefore,

constructing a binder-free and self-supporting electrode is highly desired. Recently, NiN_x[18, 64] and CuN_4[13b] on 3D self-supporting substrates have been prepared based on electrospinning technology. Specifically, the primary fibers were synthesized using an electrospinning process with the mixture solution of Cu-modified ZIF-8 and polyacrylonitrile as raw material, which was peroxidized in the air at 220 °C and subsequently carbonized under N_2 atmosphere at 900 °C to obtain CuN_4 sites on a self-supporting membrane (**Figure 2d**).[13b] This sample exhibited a through-hole structure and good mechanical properties, which can be directly used as a cathode for the CO_2RR.

Although the SACs after the heat treatment could inherit the precursor's structural properties to a certain extent, precise synthesis is relatively challenging. The wet chemistry method is a common way to prepare heterogeneous molecular catalysts. It only involves simple and mild reaction conditions that prevent structural damage to the active molecules, ensuring a high structure-activity relationship between the precursor and final sample. The active molecules can be immobilized on the carbon substrate via covalent or noncovalent intercalation for heterogeneous molecular catalysts. The noncovalent immobilization of molecular catalysts usually involves the adsorption of molecules with CO_2RR activity on the carbon substrates by liquid phase stirring or dip-coating methods. The active molecules are usually the metal porphyrin,[65] phthalocyanine[66] and polypyridine[67] based metal complexes, and the typical substrates are highly crystalline carbon materials with high conductivity and negligible CO_2RR activity, including carbon nanotubes,[65b, 66c, 68] graphene,[66b] and carbon fiber.[66a] The molecular catalysts could be modified by an organic functional group to increase their intercalation with the carbon substrate.[65a, 69] For instance, the iron triphenyl porphyrin was modified by a pyrene ring and immobilized on carbon nanotubes *via* van der Waals π-π intercalation.[65a] To further enhance the

gas diffusion and atomic loading, the highly porous and conductive 3D graphene has also been utilized as a substrate for the CO_2RR.[70] The cationic modified porphyrin iron molecules were simply mixed with negatively charged GO to form agglomerates due to the charge neutralization spontaneously. After hydrothermal reduction of the graphene oxide at 90 °C, the porphyrin Fe could be incorporated into 3D graphene hydrogels *via* electrostatic and π–π interactions.

4. Carbon-supported SACs for CO_2-to-CO conversion

As the activity of transition metals primarily originates from their unsaturated d orbital, rational selection of the active metal center is the most direct way to tune the activity and selectivity for the CO_2RR. According to the contrast experiment and theoretical calculation, Ni and Fe based MN_4 catalysts and Co-based molecular catalysts have the highest CO_2RR performance for CO production, due to their suitable adsorption energies for reaction intermediates. However, the high CO selectivity of other theoretically inactive SAC sites has also been demonstrated experimentally, which is possible due to electronic structure modulation *via* the metal-substrate intercalations. Various metal centers with different theoretical activities are discussed separately in the following section to elaborate on the activity enhancement mechanism.

4.1 Ni-based SACs

4.1.1 CO_2RR Activity of Intact NiN_4 Sites

The electroreduction of CO_2 into CO generally involves the following four elementary steps (Equations 8–11) :

$$CO_2 + e^- \rightarrow *CO_2 \quad (8)$$

$$*CO_2 + H^+ + e^- \rightarrow *COOH \quad (9)$$

$$*COOH + H^+ + e^- \rightarrow *CO + H_2O \quad (10)$$

$$*CO \rightarrow CO + * \quad (11)$$

where * denotes the active site on the catalyst surface.

The first proton-coupled electron transfer to form *COOH is generally regarded as the rate-limiting step on NiN_4 sties. The DFT calculations revealed the adsorption of COOH* on NiN_4 is thermodynamically more favorable than that of H* at high overpotential, leading to high FE for the CO_2RR. Compared with other MN_4 sites (M = Fe, Co, Cu, *etc.*), the binding of *CO on NiN_4 is relatively weak, preventing the further conversion of CO for high selectivity.[25, 71] Therefore, many NiN_4 based catalysts derived from various precursors, such as the Ni-modified MOFs,[51] the Ni-doped g-C_3N_4,[23] the mixture of Ni, N resources with graphene,[25] CNT, glucose, l-cysteine,[50] and carbon cloth, have been studied extensively as highly effective catalysts toward CO_2RR to CO. Among them, the exclusive NiN_4 on graphene achieved a current density of 28.6 mA cm^{-2} with a high CO FE of 99% at –0.81 V **(Figure 3a–c)**.[23] The in situ XAS analysis showed that the Ni K-edge of NiN_4 shifted to higher energy when exposed to CO_2 saturated electrolyte and shifted back to lower energy during the electrochemical CO_2RR process. This indicates that the activation of CO_2 molecules on NiN_4 originates from the charge transfer of Ni sites, forming chemically adsorbed $CO^{2\delta-}$ species (**Figure 3d–f**).[50]

The Tafel slope of many NiN_4 based catalysts falls into the range of 98–130 mV $decade^{-1}$, suggesting that the first proton-coupled electron transfer generates surface adsorbed *COOH species is the rate-determining step for CO evolution. This could be further confirmed by in situ electrochemical Fourier transform infrared spectroscopy (FTIR) analysis for NiN_4 catalyst. The *COOH signal gradually increased and then reached dynamic balance at a potential of –1.2 V in

CO_2 saturated $KHCO_3$ solution. Also, the S doping strategy has been used to improve the CO_2RR performance of NiN_4 sites.[72] On the one hand, the thiophene-S creates more edge defects on a carbon substrate, leading to more edge-hosted NiN_4 with optimized adsorption energies for intermediates. On the other hand, the S heteroatoms can also modulate the electronic structure of nearby NiN_4 sites and strength their *COOH adsorption.

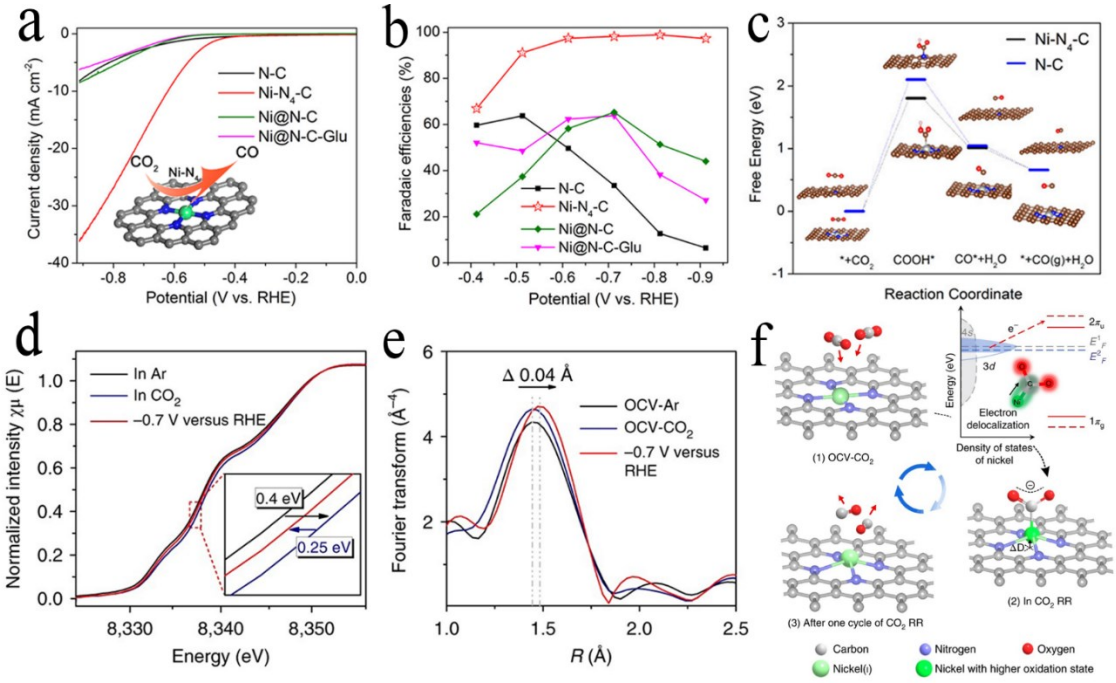

Figure 3 (a) CO_2RR LSV curves of intact NiN_4 SACs in CO_2-saturated 0.5 M $KHCO_3$ electrolyte, (b) corresponding Faraday efficiency and (c) calculated free energy diagrams of the CO_2RR on NiN_4 and metal-free N-C sites. Reproduced with permission.[23] Copyright 2017, American Chemical Society. (d–e) The EXAFS spectra for NiN_4 sites at a different working potential. (f) The structural change of the NiN_4 sites during electrochemical CO_2RR. Reproduced with permission.[50] Copyright 2018, Nature Publishing Group.

4.1.2 Optimizing the adsorption energy of intermediates on NiN_x sites

The local coordination environment plays a significant role in tuning the electronic structure of Ni SACs, leading to optimized adsorption/desorption energies of intermediates for improved CO_2RR activity and selectivity. Based on XAS spectra analysis, Koshy *et al*. suggested the CO_2RR activity of NiN_x originates from the pyrrolic-N coordinated Ni atoms in a distorted square-planar geometry, which is distinguished from the pyridine-like NiN_4 configuration by having higher HER activity.[26] Also, several different configurations were predicted to have higher CO_2RR performance compared with the intact NiN_4 configuration due to the optimized adsorption energy for *COOH and CO*, such as coordinately unsaturated NiN_2 sites, NiN_3 sites coordinated with pyrrolic N,[48] as well as the edge-hosted NiN_x sites with dangling bond-containing carbon atoms.[22b] A series of Ni-N_x-C (x = 2, 3, 4) sites with different N coordination numbers have been synthesized by controlling the pyrolytic temperature.[51] The CO_2RR activities were found to follow the trend of Ni-N_2-C > Ni-N_3-C > Ni-N_4-C, with the low-coordinated Ni-N_2-C affording a maximum CO FE of 98% and a TOF value of 1622 h^{-1} at –0.8 V. The previous work reported that the collaborative environment and electronic structure of SACs could be designed and optimized by engineering and tuning vacancy defects, which facilitates to enhance catalytic activity.[11] As shown in **Figure 4a–c**, the vacancy-defect in the NiN_3 SACs (Ni-N_3-V) can dramatically boost the electrocatalytic activity for CO production, achieving a high current density of 65 mA cm^{-2} with over 90% of CO FE at –0.9 V. The DFT results revealed the vacancy-defect could optimize the adsorption balance between the COOH* and CO* intermediates, leading to easier CO_2 activation and CO desorption on the Ni atoms (**Figure 4d–e**).

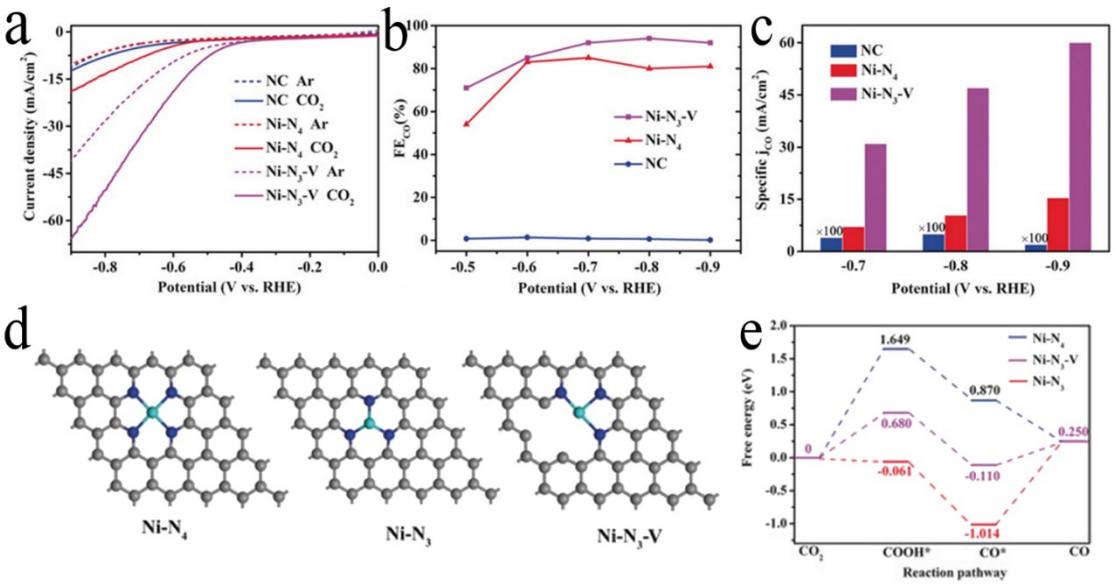

Figure 4. (a–c) The LSV curves of NiN_4 with and without vacancy defect in CO_2-saturated 0.5 M $KHCO_3$ electrolyte, (d) The schematic illustration of the possible structures of NiN_4, $Ni-N_3$, and $Ni-N_3-V$. (e) The calculated free-energy diagram for the conversion of CO_2 to CO on $Ni-N_3-V$ and other types of sites. Reproduced with permission.[11] Copyright 2019, Wiley-VCH.

4.1.3 Excluding the Influence of Ni Particles

During the synthetic process of NiN_x materials, some Ni particles may be encapsulated by carbon layers, which are difficult to remove through acid washing treatment. These Ni particles can endow the carbon substrate with significant HER activity by modulating its electronic structure and hindering CO_2RR performance. To inhibit the HER activity of the carbon substrate, Cu was introduced to trigger the charge redistribution between Ni-Cu alloy and the carbon substrate, which mostly weakened the carbon layer's binding energy for H*, thus leading to the improvement in CO selectivity.[73] The composite with NiN_x and Ni-Cu alloy exhibits a current density of 32.87 mA cm^{-2} for CO formation with 97% FE at a mild overpotential of 620 mV, superior to that of the

control sample that did not contain a Cu additive. However, another work revealed that at sufficiently high pyrolysis temperatures (>700 °C), Ni nanoparticles could catalyze the graphitization and are covered by carbon shells, which can suppress the HER by restricting electrolyte access.[26] In another case, the encapsulated Ni nanoparticles were suggested to enhance the carbon substrate's electron transfer, rather than synergy with NiN_x sites for improved electrocatalytic CO_2RR performance.[74] These different conclusions may be attributed to the difference in the thickness of the formed carbon layer because the charge delocalization between the Ni metal core and carbon shell mainly occurs when the number of carbon layers is less than three.[75]

4.1.4 Increasing the Mass Transfer Efficiency

The mass transport efficiency is another crucial factor to improve CO_2RR performance. Several kinds of rigid templates have been utilized, such as SBA-15,[57] silica[55b, 55c], and ZnO nanorods to improve mass transfer.[59] For example, the Ni-modified ZIF-MOFs were directly grown on ZnO nanorods under the liquid phase, followed by high-temperature pyrolysis to obtain the Ni SACs on rod-like carbon substrates with hierarchical porous structure. The obtained sample exhibited much enhanced current density and nearly 100% FE for CO production over a wide potential range of −0.6 to −1.0 V, due to the formation of a hierarchically porous structure with increased mass transfer efficiency.

Compared with the normal H-type cells with severe mass diffusion limitation, the flow cell-based on gas diffusion electrode facilitates the transportation of CO_2 onto the catalyst surface, thus leading to very high current densities for practical application. Zheng et al., reported the synthesis of highly active NiN_x with commercial carbon black as the support through Ni ion adsorption

followed by pyrolysis treatment.[76] The obtained catalyst was assembled into gas diffusion electrodes and applied in a flow cell, which exhibited a high current density of 83 mA cm^{-2} with a high CO selectivity of 98.4%. Möller *et al*. investigated the CO_2RR activity and CO FE of NiN_x and FeN_x catalysts in both H-cells and flow cells (**Figure 5a–f**).[77] For the H-cell based test, the FeN_x catalyst showed higher CO_2RR reactivity and CO selectivity and approached an efficiency maximum at a lower overpotential region (< 0.6 V_{RHE}). In contrast, the NiN_x catalyst continued to increase its CO production rate over the whole overpotential range (from 0.6 V_{RHE} to 0.85 V_{RHE}). This activity trend was further amplified when the catalysts were supported on a gas diffusion electrode and applied in flow cell (**Figure 5d–f**). At large current densities and overpotentials, the CO yield of NiN_x far outperformed that of the FeN_x catalyst, achieving a CO partial current density of 200 mA cm^{-2}, a CO FE around 85%, and high operational stability over 20 hours. DFT calculations revealed that the chemisorption of CO on the FeN_x moiety is too strong, leading to CO poisoning and reduced CO efficiency. In contrast, the weaker binding of CO on NiN_x facilitates the fast desorption of CO, which results in larger CO yields at larger current densities and electrode potentials. Yang *et al*.[64] reported the preparation of NiN_x on self-supported porous carbon fiber (NiSA/PCFM) for membrane electrode based CO_2RR. When integrated into a flow cell, the NiSA/PCFM could produce CO with a commercially relevant partial current density of 308.4 mA cm^{-2} and a high CO FE of 88% at –1.0 V for at least 120 hours.

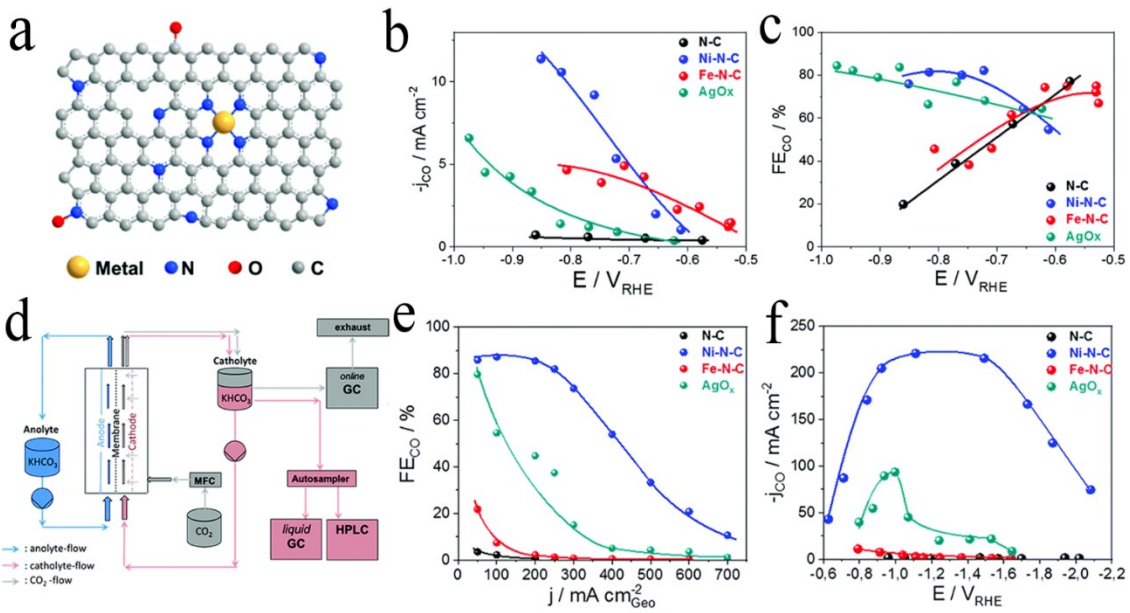

Figure 5. (a) The proposed structure of NiN_x catalyst. (b–c) The CO production current densities and corresponding CO Faradaic efficiency as a function of applied IR-corrected electrode potential for NiN_x and FeN_x catalysts. (d) The schematic illustration of the flow cell device used in this work. (e) The CO Faradaic efficiency as a function of the applied current density. (f) The CO partial current density as a function of iR-corrected CO_2 electrode potentials was assessed using a reference electrode. Reproduced with permission.[77] Copyright 2019, Royal Society of Chemistry.

4.2 Fe-based SACs

4.2.1 The Synergistic Effect between nonmetallic heteroatoms and atomic Fe species

Fe based SACs are another widely studied class of catalysts for electrochemical CO_2 reduction to CO. Several pioneer works have shown that the introduction of Fe can enhance the CO_2RR performance of N-doped carbon materials due to the formation of atomically dispersed FeN_4 moieties on the carbon substrates.[47a, 78] Compared to NiN_4 catalysts, the CO_2RR on FeN_4 catalysts

have lower onset potential for CO production, which could be explained by the stronger adsorption of *COOH intermediate on FeN_4 for CO_2 activation. However, the strong CO* binding energy on FeN_4 may inhibit the release of CO under high overpotential, causing the decrease in CO yield and selectivity at larger current densities. Thus, the FeN_4 catalysts usually reach the efficiency maximum within an overpotential range below 0.6 V, and the reported CO FE for FeN_4 is generally slightly lower than that of NiN_4 sites.[25, 71, 79] Zhang *et al*.[47a] synthesized a series of atomically dispersed Fe on N-doped graphene (Fe/NG) by pyrolysis of GO, $FeCl_3$, and NH_3 at different pyrolytic temperatures. The optimized sample prepared at 750 °C (Fe/NG-750) exhibited a maximum CO FE of 80% at a low reduction potential of –0.60 V_{RHE}. The combination of XAS analysis and control experiments confirmed the catalytic activity is positively correlated with the atomically dispersed Fe of a FeN_4 based configuration. The N heteroatoms on graphene also have a positive contribution towards the CO_2RR performance. The DFT calculations revealed the potential limiting step on FeN_4 is the formation of *COOH intermediates on FeN_4 and the fact that the nearby N heteroatoms on graphene improve the catalytic activity of the FeN_4 moieties by lowering the energy barrier for both COOH* formation and CO* desorption. Asset *et al*.[80] showed that both the N-doped graphene with and without FeN_x sites could achieve a FE up to ~50% at a low reaction potential of –0.35 V_{RHE}. The near-ambient pressure X-ray photoelectron spectroscopy analysis confirmed that the pyridinic and pyrrolic N are preferential adsorption sites for the CO_2, which indicates that the N heteroatoms on FeN_4 based materials may also serve as critical active sites for the CO_2RR at low overpotentials.

Wang *et al*.[81] found that the distribution of FeN_x on the carbon frameworks can be tuned by using different Fe precursors. To be specific, cyano-modified FePc is easy to incorporate into ZIF-8, resulting in more FeN_x sites inside carbon frameworks ($FePc(CN)_8$/ZIF-8). In contrast, the

$Fe(NO_3)_3$ can enrich on the surface of ZIF-8 to produce more FeN_x exposed on the carbon surface. The $FePc(CN)_8$/ZIF-8 exhibited a reduction current density of 5 mA/cm^2 at −0.46 V with a CO FE of 94%, superior to most FeN_x based catalysts (**Figure 6a–c**). Similar to the calculation results from Zhang *et al.*,[47a] the DFT calculations revealed that N heteroatoms near FeN_x sites could weaken the binding energy of CO* intermediates for more accessible CO release, which may explain the higher activity of inner FeN_x sites, which are surrounded by more N heteroatoms when compared to surface FeN_x sites (**Figure 6d–e**).[81] In addition to N heteroatoms, the synergistic effect between FeN_4 sites and the S heteroatoms has been investigated.[82] The introduction of S heteroatoms could act as an electron donor to increase Fe atoms' charge density, strengthening the adsorption energy of rate-limiting COOH* intermediate, thus increasing the CO_2RR activity.

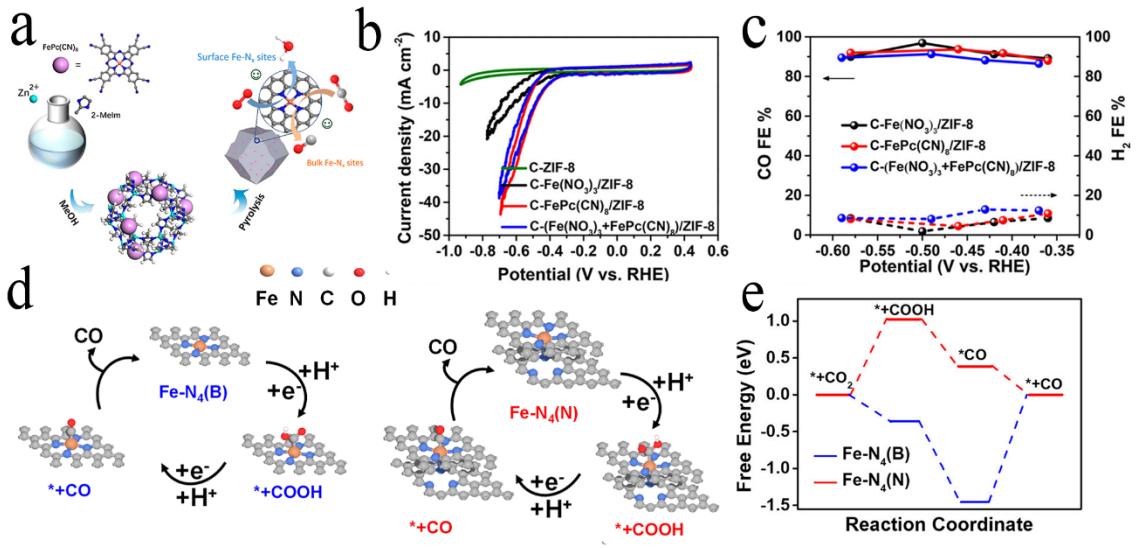

Figure 6. (a) Schematic illustration of the synthetic method for FeN_x sites embedded into carbon frameworks from cyano-modified FePc and ZIF-8. (b) The cyclic voltammograms at 20 mV s^{-1} of C-$FePc(CN)_8$/ZIF-8 and the control samples measured in 0.5 M $KHCO_3$ solution saturated with

CO_2. (c) The Faradaic efficiency of C-FePc$(CN)_8$/ZIF-8 and the control samples for CO and H_2 production. Reproduced with permission.[81] Copyright 2019, American Chemical Society.

4.2.2 The Activity of different FeN_x Configuration

Although various FeN_x configurations have been identified and recognized as active sites, more systematic investigations concerning the effect of synthetic conditions on morphology, structure, and activity of the catalysts are still needed to achieve optimized CO_2RR performance. To address this issue, we developed a controllable synthesis method to obtain a series of FeN_4 model catalysts, as shown in **Figure 7**, and comprehensively studied the effect of particle size (**Figure 7a**), Fe content (**Figure 7b**), and Fe–N bond structure on CO_2RR performance.[83] This method involves the synthesis of N-doped carbon frameworks through the carbonization of ZIF-8 and followed by subsequent thermal activation to form FeN_4 sites. It separates the Fe–N bond formation from complex carbonization and N doping process, which facilitates the control of FeN_4 formation and enables the exclusive investigation of the impact of the thermal activation conditions on the structural evolution of FeN_4 sites. The combination of XAS and DFT analysis revealed that the higher thermal activation temperature could significantly increase the CO_2RR activity and selectivity by shortening the Fe–N bond lengths in FeN_4 sites to optimize the adsorption for reaction intermediates. Local contraction strain of the Fe-N bond with shortened length can be generated beyond 400 °C. However, too high temperatures, *e.g.,* 1100 °C, can cause the decomposition of FeN_4 sites, leading to a decrease in CO selectivity (**Figure 7c-d**). Also, a more massive strain (*e.g.*, -2%) would be more beneficial to the HER, thus scarifying CO selectivity (**Figure 7e-g**).

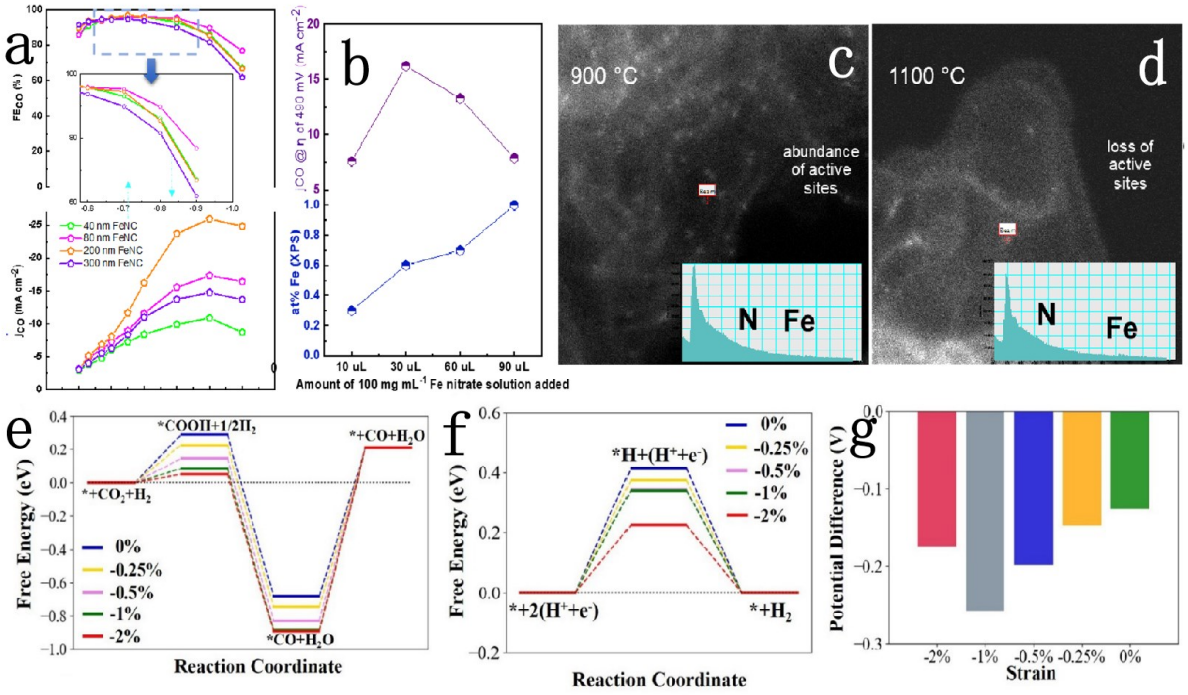

Figure 7. (a) CO faradaic efficiency of different-sized Fe-N-C. (b) Correlation between the variation of Fe doping and its corresponding catalytic performance as parameterized by the CO partial current density. HAADF-STEM and corresponding EELS analysis of atomic Fe for samples thermally-activated at (c) 900 °C and (d) 1100 °C. (e) Predicted CO_2RR free energy evolution on FeN_4 sites with varying strain. (f) Predicted free energy evolution of HER on FeN_4 sites with varying strain. (g) Variation of the difference between the limiting potentials of HER and CO_2RR as a function of the strain in FeN_4 sites. Reproduced with permission.[83] Copyright 2020, Wiley-VCH.

Also, the geometric structure and coordination environment of FeN_x sites are crucial factors in modulating the electronic structure of Fe centers for improved CO_2RR performance. Qin *et al.*[84] showed that FeN_x catalysts could start to catalyze the CO_2RR at a low reduction potential of –0.2 V_{RHE}, and a high CO FE (>83%) can be maintained in the range from –0.3 to –0.6 V_{RHE}, with

a maximum value of 93.5% at –0.5 V_{RHE}. Both in-situ attenuated total reflection infrared (ATR-IR) spectroscopy and theoretical calculations suggest that the bulk FeN_4 moieties are poisoned by strongly adsorbed CO and should not be the actual active sites for CO production. The edge-located Fe-N_4 sites with dangling bond-containing carbon atoms should be responsible for the high CO_2RR activity due to the low activation energy in the dissociation of the *COOH intermediate. In contrast, the activation barrier for competitive HER is higher (**Figure 8a–c**). Also, STEM and XAS analyses further support the edge-hosted FeN_{2+2} model, with atomically dispersed FeN_4 sites uniformly distributed along the edges of the porous carbon matrix. Based on experimental spectra combined with theoretical calculations, Sun *et al.*[55a] proposed another possible model for the CO_2RR, a porphyritic FeN_4 configuration with an axial –OH ligand binding on the Fe center. The porphyritic coordination environment and the –OH moieties decrease the free energy barriers of *COOH formation and destabilize the adsorption of *H, thus endowing Fe centers with high CO_2RR activity. A similar configuration has also been identified and regarded as a possible active site for the CO_2RR[56] and other electrocatalytic reactions.[85]

Besides, Wang *et al.*[44] synthesized a series of MOF derived FeN_x catalysts and investigated the influence of particle sizes and pyrolytic temperature on the FeN_x configuration and CO_2RR activity (**Figure 8d–f**). The optimized Fe_1NC/S_1-1000 samples prepared at 1000 °C exhibit excellent CO_2RR performance, with a current density of 6.4 mA cm^{-2} and a CO FE of 96% at –0.5 V_{RHE}, as well as excellent stability during 48 hours of continuous operation. The enhanced CO_2RR activity was attributed to the formation of FeN_3V (V: vacancy) sites that balance the energy barriers between CO_2-to-*COOH, *COOH-to-*CO, and *CO-to-CO conversions. Also, the formation of more graphitic N under high-temperature conditions (*e.g.*, 1000 °C) could induce

charge redistribution to improve the *COOH adsorption and enhance the electron transport, which would also have a positive effect on CO_2RR.[44, 86]

In addition to the vacancy defect, N coordination number, local strain, electronic structure, and CO_2RR activity of FeN_x sites were also found to be highly related to the type of coordinated N atoms.[9, 24a] Based on in-situ XAS spectra analysis, Gu *et al*.[9] revealed that the high activity and stability of FeN_x for the CO_2RR might originate from Fe^{3+} atoms coordinated by four pyrrole-type N atoms. During electrocatalysis, the pyrrole-type N ligands help maintain the Fe atom's +3 oxidation state with faster CO_2 adsorption and weaker CO absorption. In contrast, pyridine-type N coordinated Fe atoms tend to be reduced to Fe^{2+}, which has poor CO_2RR performance. It should be noticed that the preservation of the +3 oxidation state during CO_2 electroreduction is inconsistent with the CO_2RR mechanism of molecular Fe catalysts, which involves the formation of highly reduced, low-valence Fe species. This indicates the electronic structure of FeN_x sites may be further tuned by metal-substrate intercalation.

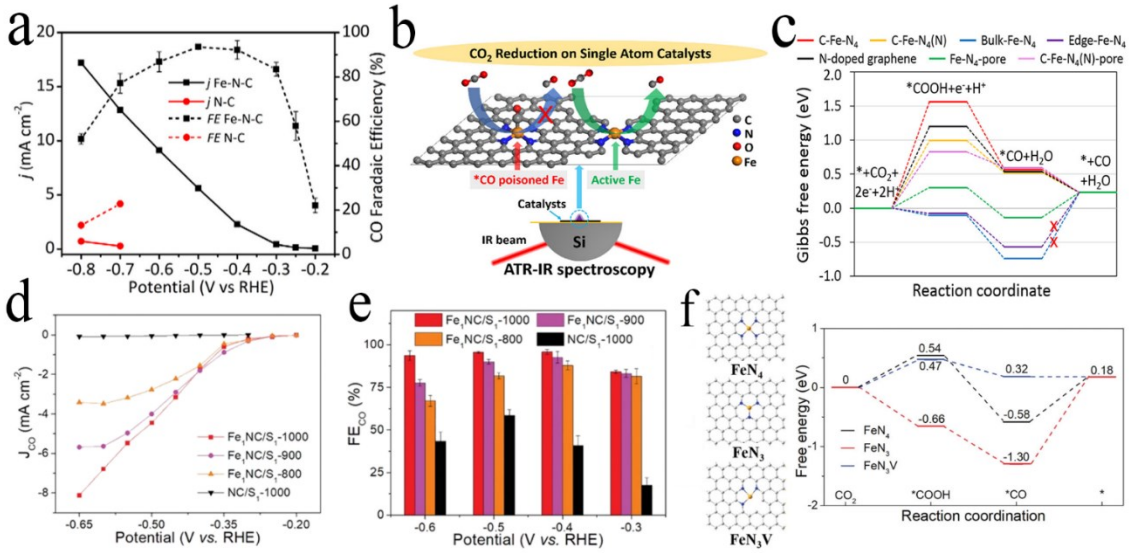

Figure 8. (a) The current densities and CO FE as a function of applied reduction potential for FeN_{2+2} catalyst. (b) The schematic illustration of CO_2RR on FeN_{2+2} sites. (c) The calculated free energy diagrams of the CO_2RR on Fe SACs with different configurations. Reproduced with permission.[84] Copyright 2019, American Chemical Society. (d) The current densities and (e) FE for CO production on Fe_1NC/S_1-1000 and control samples prepared at different pyrolytic temperatures. (f) The calculated free-energy diagrams for CO_2RR pathway of FeN_4, FeN_3, and FeN_3V moieties. Reproduced with permission.[44] Copyright 2020, Wiley-VCH.

4.3 Co-based SACs

4.3.1 Triggering the CO_2RR activity of CoN_x sites

Unlike Ni and Fe based MN_x catalysts that possess relatively high theoretical activity, the influence of the local coordination environment on the CO_2RR activity of CoN_x sites is still elusive. According to previous theoretical and experimental data, the intact CoN_4 catalysts on N-doped graphene have relatively low selectivity for the CO_2RR due to its high activity for H_2 evolution.[25] However, the CO_2RR activity of CoN_x catalysts could be triggered by engineering the N coordination number or improving the porous structure of the carbon substrates. For instance, Wang *et al.* discovered that increasing the pyrolytic temperature from 800 to 1000 ºC can lead to the conversion of CoN_4 into CoN_2 sites with higher CO_2RR activity.[8] The optimized CoN_2 catalyst exhibited a current density of 18.1 mA cm^{-2} with a high CO FE of 94% at an overpotential of 520 mV. The same trend of influence for pyrolytic temperature on N coordination has also been observed in other work. However, the CoN_4 sites prepared at lower temperatures were found to exhibit better CO_2RR performance than the CoN_x sites with decreased N coordination number.[87]

These results indicate that the other factors and the local coordination environment also greatly influence the CO_2RR activity of CoN_x catalysts.

Improving the carbon substrate's porosity is another efficient way to improve CO_2RR activity and selectivity for CoN_x sites. Recently porosity-induced enhancement in CO selectivity for MOFs-derived MN_x catalysts has been reported.[88] Using SiO_2 as the template, a series of MN_x on N-doped carbon with hierarchical pore structure were synthesized. The mesopores and macropores rather than the micropores may be responsible for the improved CO selectivity because the control sample without SiO_2 contains a larger micropore area but low selectivity. The intact CoN_4 sites on 3D self-supported nanofibers have also been synthesized for the CO_2RR based on electrospinning technology.[89] ZIF-8 was used as a porogen to create mesopores in the 3D carbon substrates, which plays a crucial part in achieving high CO_2RR activity. Due to the improved utilization of single atoms and the mass transfer efficiency, the optimized samples achieved a current density of 67 mA cm^{-2} with a CO FE of 91% in a typical H-type cell, and a current density of 211 mA cm^{-2} with a CO FE of 92% in a flow cell.

4.3.2 Co-based Heterogeneous Molecular Catalysts

As opposed to the controversial activity of CoN_x catalysts, various Co-based porphyrin and phthalocyanine (CoPc) molecules immobilized on highly conductive carbon substrates have been profoundly demonstrated as effective heterogeneous SACs for electrochemical CO_2 reduction to CO. The noncovalent immobilization *via* π-π intercalation is a simple and effective method to prepare these catalysts. Several carbon substrates with extended π-conjugated structures have been developed, including the CNT,[65b, 68] graphene,[66b] and 3D carbon cloth.[33, 66a] Compared to reduced GO (RGO) or carbon black, the CNT was more effective for active enhancement. A higher

degree of graphitization enables stronger π π interactions and better electron conduction. Cobalt meso-tetraphenylporphyrin (CoTPP) was selected as a model catalyst under both homogeneous and heterogeneous conditions to investigate the effect of immobilization on CO2RR performance experimentally.[68] After being immobilized on single-walled CNT, the heterogeneous CoTPP based catalysts showed greatly improved CO_2RR activity and selectivity, with a CO FE of 91% at an overpotential of 550 mV. The theoretical calculations and experiments suggested that the CNT's curvature plays an essential role in tuning the active Co molecules' activity and selectivity. Compared to single-walled CNT, the multiwalled CNT with a larger diameter and smaller curvature provides stronger π-π interaction due to better interfacial contact between the Co porphyrin ring and CNTs, which inhibits the self-aggregation of Co porphyrin molecules for better performance.[90] The unique electronic intercalation between multiwalled CNT and Co porphyrin may also optimize the adsorption energy of COOH* and CO* intermediates on Co centers to increase the CO selectivity.[91] Several CoPc molecules have been immobilized on multiwalled CNT to form heterogeneous molecular catalysts for the CO_2RR.[68, 92] The catalytic performance could be further improved by introducing cyano-groups to the CoPc molecule as the electron-withdrawing, which facilitates the formation of active Co (I) species during the CO_2RR process.[29] The resulting heterogeneous catalyst exhibited a CO FE of 95% in a wide potential range. The current density and turnover frequency reached 15.0 mA cm^{-2} and 4.1 s^{-1}, respectively, at an overpotential of 0.52 V in a near-neutral aqueous solution. The positively charged trimethyl ammonium is another effective functional group that can increase the CO_2RR performance of CoPc over a broad pH range from 4 to 14. The resulting sample achieved a CO selectivity of 95%, excellent stability, along with a maximum partial current density of 165 mA cm^{-2} at −0.92 V_{RHE} in a flow cell. The enhanced reactivity for CO_2 to CO conversion may be attributed to the through-

space interactions between the positive charge of the trimethyl ammonium group and the partial negative charge of CO_2, which favors the binding of CO_2 molecules on Co centers and the subsequent C–O bond cleavage for CO formation.

Covalent immobilization *via* axial coordination between Co atoms and heteroatoms on carbon substrates can mitigate aggregation and modulate the electronic structure of Co SACs to enhance activity and stability. Pan *et al*.[93] designed an atomically dispersed CoN_5 electrocatalyst with Co phthalocyanine sites anchored on hollow N-doped porous carbon spheres *via* the Co−N coordination, which achieved a 15.5-fold enhancement in activity compared to original CoPc. Furthermore, the CO FE of CoN_5 based catalyst reached 99.2% and 99.4% at –0.73 and –0.79 $V_{RHE,}$ respectively. The improved performance should be attributed to the rapid formation of the critical intermediate COOH* and CO's desorption on CoN_5 sites. Aside from selecting appropriate active sites, the electrocatalytic activity on heterogeneous molecular catalysts also relies on the electronic intercalation between the metal centers and the substrates. Wang *et al*.[28a] synthesized two heterogeneous Co SACs by immobilizing planar Co^{II}-2,3-naphthalocyanine complexes (NapCo) on graphene doped with N, S, O heteroatoms and investigated the linkage effects. A systematic study revealed that graphitic sulfoxide and carboxyl dopants on graphene were the efficient binding sites for the immobilization of NapCo *via* axial coordination. Compared to carboxyl dopants, the sulfoxide dopants further improved the electron communication between NapCo and graphene, optimizing the adsorption balance for reaction intermediates (**Figure 9a–b**). This leads to an increase in TOF by about three times for CO production with a FE up to 97 %, in addition to improved stability (**Figure 9c–e**).

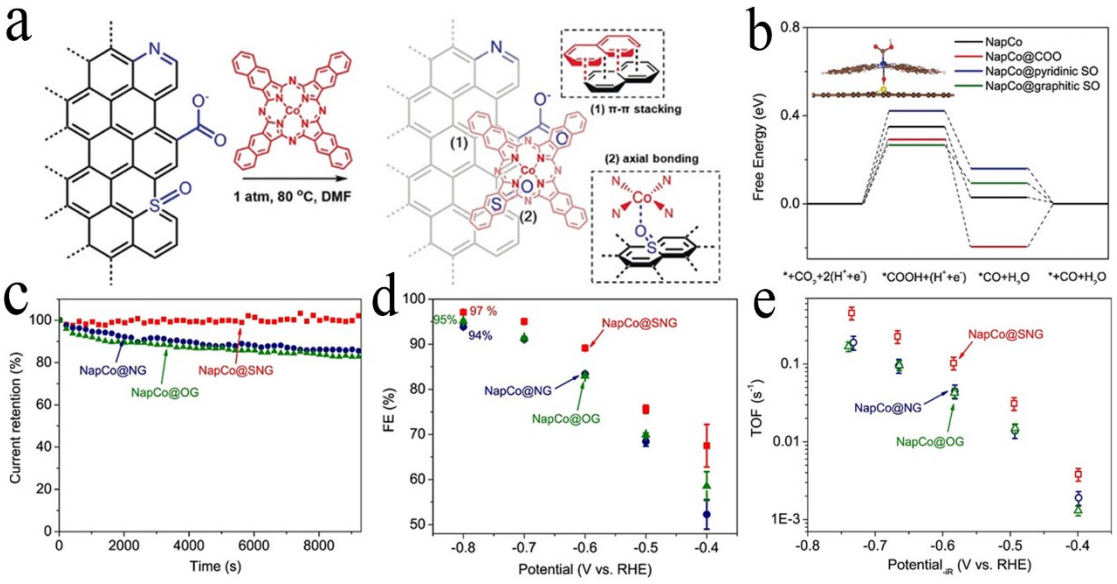

Figure 9. (a) Immobilization of NapCo onto doped graphene *via* π–π intercalation and coordination with heteroatoms. (b) The calculated free energy diagrams of CO_2RR on pure NapCo and NapCo coordinated with COO, pyridinic SO and graphitic SO doped graphene. (c) The CO FE, (d) corresponding chronoamperometric curves and (e) TOFs for NapCo immobilized on O doped (NapCo@OG), N/O doped (NapCo@NG) and N/S/O doped (NapCo@SNG) graphene, respectively. Reproduced with permission.[28a] Copyright 2019, Wiley-VCH.

4.4 Other Non-noble Metal-based SACs

Other non-noble metal-based MN_x sites, including Zn,[53, 94] Mn,[95] Bi,[61] and Cu,[52] have also been synthesized and exhibited notable activity for electrochemical CO_2 reduction to CO. Zn element is usually used as a porogen to create micropores and inhibit the agglomeration of single metal atoms on carbon substrates during pyrolysis. Recently, the CO_2RR activity of Zn based SACs was investigated. The N-anchored Zn SACs were prepared by pyrolysis of urea, zinc acetate,

and carbon black at 1000 °C.[14] The obtained samples are capable of selectively catalyzing the reduction of CO_2 to CO, achieving a current density of –4.8 mA cm^{-2} with a high FE of ~95% at –0.43 V and remarkable durability over 75 hours. Further experimental and DFT results indicate that the ZnN_4 moiety is the leading active site for the CO_2RR due to its low free energy barrier that promotes the rate-controlling formation of *COOH intermediates. ZIF-8 is an ideal precursor to synthesize atomically dispersed MN_x sites on N-doped carbon substrates, but the residual Zn species is difficult to remove after pyrolysis at high temperatures completely. Therefore, the fabrication of pure and atomically dispersed metal active sites based on new types of MOFs is needed to isolate the influence of Zn. Through the thermal emission and adsorption strategy, the exclusive BiN_4 site on N-doped carbon networks (Bi SAs/NC) with hierarchical porosity was synthesized by pyrolysis of N-free Bi-based MOFs and dicyandiamide for efficient CO_2 reduction to CO.[61] The Bi SAs/NC exhibited high intrinsic CO_2RR activity for CO conversion, with a current density of 5.1 mA cm^{-2} and a high FE of 97% at a low potential of –0.5 V_{RHE}. By using Cl-containing $MnCl_2$ and ethylenediamine as a precursor, the MnN_4Cl with an axial Cl ligand has been synthesized.[96] Due to the electronic modulation *via* Cl coordination, the MnN_4Cl showed much improved CO_2RR performance, with a maximum CO FE of 97% and considerable stability over 12 hours. The in-situ XAS analysis revealed the CO_2RR activity originates from the charge transfer from Mn to CO_2 to form a $CO_2^{\delta-}$ species and then undergoes CO_2 reduction. In another work, the CO_2RR activity of Cu based SACs was improved by increasing the pyrolytic temperature to form coordinatively unsaturated CuN_2 sites.[52] Compared to intact CuN_4 sites, the shorter bond lengths of Cu−N bonds in CuN_2 favors the electron transfer from Cu center to *CO_2, thus boosting the formation of *COOH and *CO for better CO_2RR activity.

Several heterogeneous molecular catalysts, such as Mn[67b] and Re,[97] have been synthesized. The $MnBr(bpy)(CO)_3$ complex was modified by a pyrene unite and immobilized onto CNT *via* π-π interaction for electrocatalytic CO_2RR. This catalyst exhibited a turnover number of 1790 ± 290 for CO at an overpotential of 550 mV. The in-situ UV−vis and ATR-IR spectra revealed that the formation of dimeric Mn^0 species at high Mn molecule loading should be responsible for the CO formation. Also, the Re based complexes were anchored onto glassy carbon electrode *via* pyrazine conjugation reaction to achieve improved CO_2RR performance [97a] due to the strong electronic coupling between the molecular active sites and the electrode surface.[98]

4.5 Dual-Metal Sites

The dual-metal sites with two metal atoms located adjacently on the same carbon substrate, which have been experimentally observed, could be regarded as a derivative structure of SACs. The Fe–Fe,[99] Fe–Cu[100] and Ni–Co[101] based dual-metal sites have been theoretically predicted to be active for electrochemical conversion of CO_2 into CO, HCOOH, CH_4, and CH_3CH_2OH. The dual-metal configurations can trigger unique synergetic interaction by tuning the electronic and geometric effects of active sites, which allows for alternative reaction paths to decrease the activation barriers of CO_2RR. Up to now, several kinds of dual-metal catalysts, such as Ni–Fe,[42] Cu–Fe,[43] and Zn–Co,[102] have been experimentally demonstrated as efficient catalysts toward CO_2RR to CO. The Ni–Fe sites were synthesized by pyrolysis of Ni, Fe modified ZIF at 1000 ^oC.[42] The DFT calculation suggested that the Ni–Fe sites could be activated *via* adsorption of a CO molecule during the CO_2RR process, which has a lower reaction barrier for the formation of COOH* and desorption of CO, thus leading to high CO_2RR activity and CO selectivity. The Zn–Co sites have been obtained by pyrolysis of the mixture of Zn^{2+}, Co^{2+}, and conductive carbon black

at a temperature below the boiling point of Zn (*e.g.,* 700 °C).[102] The electronic intercalation between Zn and Co atoms could be observed in both X-ray photoelectron spectroscopy (XPS) and XAS analysis. This catalyst exhibited a CO FE of 93.2% and a CO partial current density of ~26 mA cm^{-2} at 0.5 V_{RHE} during a 30-hours test. According to the DFT calculation, the Co–Zn configuration can optimize the binding energy of *COOH intermediate on Zn sites, thus promoting the CO formation.

5 Other C_1 and C_2 Products beyond CO

Generating other products beyond CO is of great significance for CO_2 reduction. Compared to CO production, the conversion of CO_2 into other multielectron products involves a more complicated reaction pathway, which usually suffers from the severe problem of catalytic selectivity. Despite being in its infancy, several kinds of carbon-supported SACs have demonstrated themselves as potential catalysts for CO_2 conversion to other C_1 and C_2 products, which are summarized in the following section.

5.1 Production of Formate

Although formate is the most straightforward liquid product for CO_2 reduction *via* a 2-electron pathway, only a few works reported the selective reduction of CO_2 to formate due to the higher CO selectivity for most carbon-supported SACs. The Sn, Mo, and In based MN_x sites have catalyzed the CO_2 to formate conversion with effective selectivity. Zu *et al*. successfully synthesized atomically dispersed $Sn^{\delta+}$ sites on N-doped graphene at a kilogram-scale based on a quick freeze–vacuum drying–calcination method.[10] This catalyst exhibited excellent activity and stability for formate generation, with a low onset overpotential of 60 mV, a maximum formate FE

of 74.3% at −1.6 V_{SCE}, and over 200 hours of operational stability without deactivation. The combination FT-IR analysis and DFT calculations revealed that the positively charged Sn atoms enable the CO_2 activation and protonation to spontaneously through stabilizing $CO_2^{\bullet-}$* and $HCOO^-$*. The N-doping facilitates the rate-limiting formate desorption step through weakening the bonding strength between Sn and $HCOO^-$*, explaining the unique selectivity of SnN_x sites for formate production. The atomically dispersed Mo sites loaded onto ultrathin N-doped graphene was also prepared and investigated concerning electrocatalytic activity and selectivity for formate production.[103] With the aid of 4 mol % ionic liquid, the catalyst presented a high formate production rate of 747 mmol g_{cat}^{-1} h^{-1}, which is 100% higher than that of Mo-free N-doped graphene. Based on the MOF-derived method, the exclusive InN_4 sites have also been synthesized for the CO_2RR to formate, which exhibited a current density of 8.87 mA cm^{-2} at −0.65 V with a formate FE of 96 %.[104]

5.2 Production of Methanol

The 6-electron electrochemical reduction of CO_2 into methanol is of great research significance because methanol possesses a high energy density for energy storage and is a significant precursor for many high-value chemicals. The CuN_4 catalyst has been reported to catalyze the production of methanol with relatively high effectivity.[13b] The atomically dispersed CuN_4 on through-hole carbon nanofibers (CuSAs/TCNFs) was synthesized by pyrolysis of an electrospun polyacrylonitrile membrane and Cu ions with ZIF-8 as porogen. This 3D free-standing CuSAs/TCNF could be directly used as a cathode for the CO_2RR, which can generate methanol with a FE of 44% (**Figure 10a**) and long-term stability over 50 hours. The introduction of a through-hole structure could increase the current density (**Figure 10b**) but have a negligible

influence in methanol selectivity. The methanol and CO are nearly the only liquid- and gas-phase products, respectively, which indicates that CO* may be the key intermediate for methanol formation. The involved mechanism was further studied by DFT calculations (**Figure 10c–e**). The catalytic site should not bind the CO* intermediate too weakly nor too strongly to enable more profound CO_2 reduction. Unlike the NiN_4 moiety with its high CO selectivity, the CuN_4 has relatively moderate adsorption energy for *CO intermediate, which facilitates the further reduction of *CO intermediates rather than being released as CO. Besides, the formation of CHOH* on CuN_4 sites has a lower energy barrier than that of C*, which is a crucial intermediate for CH_4 formation. Thus, the CuSAs/TCNF catalyst tends to generate CH_3OH instead of CH_4.

In addition to MN_x based catalysts, the heterogeneous molecular catalysts, *e.g.*, CoPc immobilized on carbon substrates, have also been demonstrated effective for electrochemical CO_2 reduction to methanol.[13a] Both the local coordination environment and the carbon substrate's intercalation are significant to trigger the methanol selectivity for Co atoms. When immobilized on CNT, the CoPc, a catalyst previously used to reduce CO_2 to primarily CO, can catalyze the electrochemical CO_2 reduction to methanol with a 44% selectivity and a partial current density of 10.6 mA cm^{-2} at −0.94 V_{RHE}. Such a methanol selectivity cannot be achieved if the CNT substrate or the phthalocyanine ligand is replaced with another species. Considering the moderate adsorption energy of CO molecules and the significant catalytic efficiency for CO reduction to MeOH on this catalyst, the authors suggested that CO_2 may first undergo a 2-electron reduction to CO, which continues to be reduced to methanol through a 4-electron/proton process. Also, the introduction of an electron-donating amino functional group on the phthalocyanine can increase the catalyst's durability by inhibiting the hydrogenation of the phthalocyanine ligand during CO_2RR.

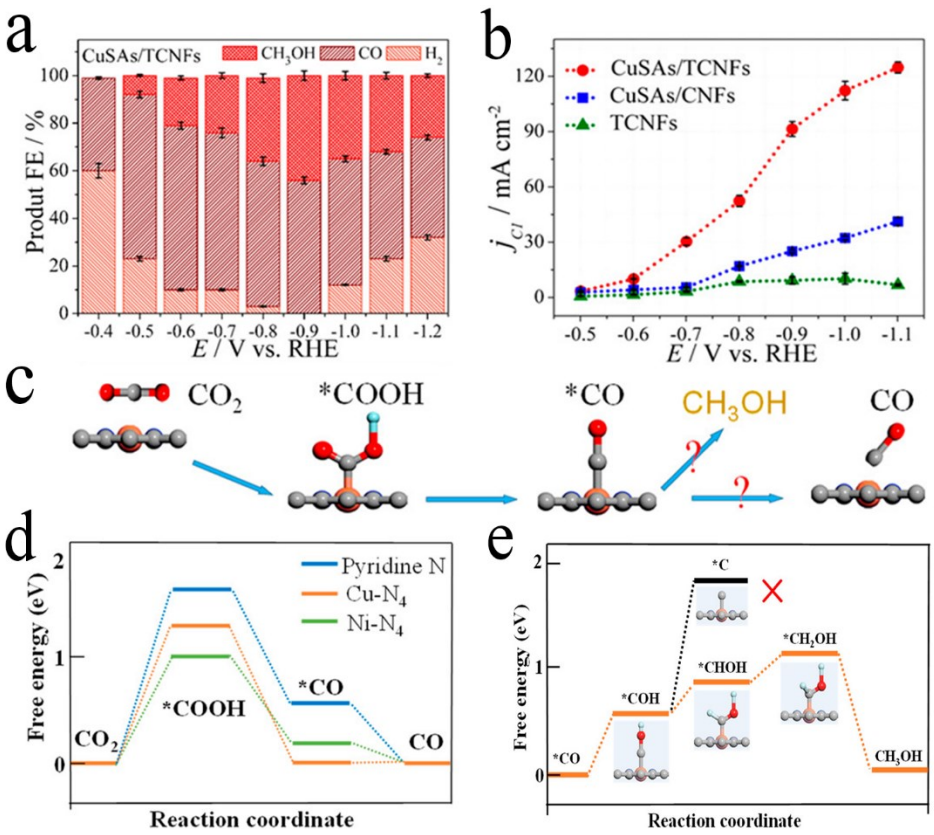

Figure 10. (a) The FE for all products on CuSAs/TCNFs catalyst. (b) The CO partial current density for CuSAs/TCNFs and the control samples. (c) The schematic illustration of the proposed atomic structure of CuSAs/TCNFs and reaction paths for CO_2 electroreduction. (d) The calculated free energy diagram for CO_2 to CO conversion on different active sites. (e) The calculated free energy diagram for CO to CH_3OH conversion on CuN_4 site. Reproduced with permission.[13b] Copyright 2019, American Chemical Society.

5.3 Production of Methane

Up to now, only a few studies have reported the electrochemical reduction of CO_2 to CH_4 on carbon-supported SACs, including several Cu,[16] Co,[105] Fe,[78, 106] and Zn[14] based MN_x catalysts,

as well as Cu-based[107] heterogeneous molecular catalysts. Among them, ZnN_4 on microporous N-doped carbon (SA-Zn/MNC) derived from ZIF-8 exhibited the highest activity and selectivity for CH_4 production (**Figure 11**).[14] The FE for CH_4 production over SA-Zn/MNC reached a maximum value of 85% with a partial current density of −31.8 mA cm^{-2} at −1.8 V_{SCE} and considerable stability over 35 hours of testing. The combined FE of CH_4, CO, and H_2 was ~100% over the entire potential range, and no other products were detected. According to previous studies, many MN_x tends to bond the C atom of CO_2, which leads to the sequent protonation of O atoms to form *COOH with a low energy barrier for CO production. If the oxygen atom of CO_2 binds to the active sites, the C atom would be protonated to form *OCHO. The DFT calculations reveal that the oxygen-binding intermediate *OCHO is more stable than the carbon-binding intermediate *COOH for ZnN_4 sites, which blocks the generation of CO and promotes the formation of CH_4.

For heterogeneous molecular catalysts, Weng *et al.*[107a] revealed the catalytic mechanism of Cu phthalocyanine supported on CNT involves the reversible structural and oxidation state changes of Cu atoms to form ~2 nm Cu clusters as the active sites for methane production. As confirmed by in-situ XAS analysis, a similar phenomenon was not observed on the Cu based MOF or complexes with a non-conjugated ligand. This indicates that the reversible restructuring behavior and catalytic activity is positively related to the π-conjugated coordination environment provided by the phthalocyanine molecule.

Several works have observed methane as a minor reaction product on FeN_x sites, and the mechanism involved has been investigated.[78, 106, 108] In addition to directly catalyzing the CO_2 to CH_4 conversion *via* 8-electron/ proton pathway, the FeN_x can first catalyze the formation of CH_2O, which undergoes subsequent conversion from CH_2O to CH_4 *via* a 4-electron/proton pathway. On

the contrary, CH_3OH appears to be an end product aside from the non-CH2O pathway's methane.[106a] Although both decreasing the pH and adding the phosphate-containing electrolytes were found to promote the CH_4 formation for FeN_x catalysts, the overall CH_4 selectivity (< 2%) is still far from practical applications due to the predominant production of H_2.

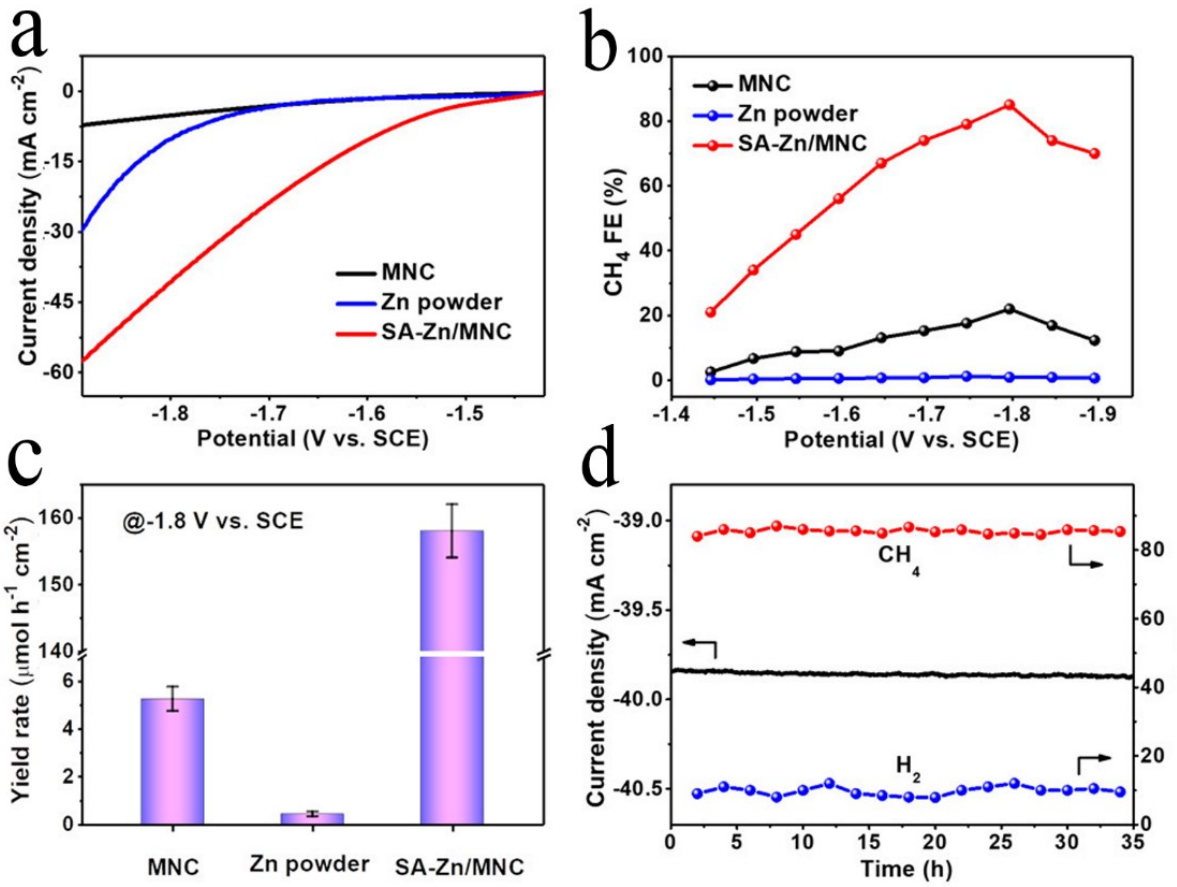

Figure 11. (a) The LSV curves for SA-Zn/MNC, MNC and Zn powder. (b) The FE for CH_4 at different applied potentials. (c) The yield rates for CH_4 at −1.8 V_{SCE}. (d) The stability test for SA-Zn/MNC at −1.8 V_{SCE}. Reproduced with permission.[14] Copyright 2020, American Chemical Society.

5.4 Production of C_2 species

Various C_2 products from the CO_2RR are incredibly valuable. Among the carbon-supported SACs, up to now, Cu was known as the only metal that can catalyze the formation of these C_2 products, such as ethanol,[15, 17, 109] ethylene,[16, 37b, 110] and ethane.[17] The catalytic mechanism is still controversial, involving the reversible transformation into Cu clusters [15, 37b, 109-110] the dual Cu atomic catalysis,[16] and the synergism between Cu atoms and adjacent metal-free heteroatoms.[17, 111]

As the C_2 reaction pathway involves forming the C–C bond, it is likely mediated by two active sites rather than a mononuclear Cu center. The work by Karapinar *et al*.[15] revealed that the atomically dispersed CuN_x sites could reversibly convert into Cu clusters during CO_2RR, which are suggested as the real active sites for ethanol production. Using 0.1 M $CsHCO_3$ as an electrolyte, this catalyst could catalyze the CO_2RR to produce ethanol with a 55% FE at – 1.2 V_{RHE}. Recently, Xu *et al*. reported the synthesis of O-coordinated Cu SACs on commercial carbon black by an amalgamated Cu–Li method.[109] The optimized catalyst with 0.4 wt% Cu loading exhibited high ethanol selectivity, excellent ethanol FE of ~91% at −0.7 V_{RHE} with negligible activity, and selectivity changes over 16 hours testing (**Figure 12a–c**). As shown by in-situ XAS analysis (**Figure 12d–h**), the atomically dispersed Cu^{2+} atoms undergo a dynamic transformation to zero-valence state ultrasmall Cu_3 or Cu_4 clusters as soon as the cell voltage is applied at –0.7 V. The Cu clusters will be ligated by the hydroxyl group on the carbon substrate and serve as the transient active site for CO_2-to-ethanol conversion. The metallic Cu^0 phase disappeared and restored to the initial Cu^{2+} phase once the cell voltage was switched off, indicating this transformation process's reversibility. Meanwhile, the hydroxyl group on the carbon substrate plays a significant role in

stabilizing the Cu cluster and modulates its electronic structure to optimize the adsorption properties, leading to improved activity and selectivity compared to the N-coordinated CuN_x sites. Similar potential-driven restructuring behavior has also been observed for other types of carbon-supported Cu SACs, including Cu atoms anchored on COFs[37b] and molecular Cu complexes immobilized on mesoporous carbon,[110a] in which the in-situ formed Cu clusters rather than single-atom sites are responsible for the formation of C_2H_4. For COF based Cu SACs,[37b] a significant increase in selectivity for producing C_2 chemicals could be achieved when the catalyst is exposed to a CO atmosphere instead of CO_2, which could be explained by increased CO coverage and enhanced local pH around catalytic sites in a CO-saturated electrolyte, leading to accelerative C−C coupling reactions. Also, the acetate that is rare for carbon-supported Cu SACs was observed, which indicates that the intercalation from the COF skeleton plays a unique role in tuning the CO_2RR selectivity of the Cu clusters.

Synergistic catalysis between two neighboring Cu atoms is another possible mechanism for the generation of C_2 products. Guan *et al*.[16] revealed the catalytic selectivity of a CuN_x based catalyst depends highly on the Cu atomic density. When the Cu atomic concentration is lower than 2.4 $\%_{mol}$, the isolated CuN_4 sites favored the formation of CH_4. At a high Cu concentration of 4.9 $\%_{mol}$, the distance between adjacent CuN_x sites is close enough to trigger C–C coupling and produce C_2H_4. For the g-C_3N_4 supported Cu SACs,[17] the C atoms could act as additional adsorption sites for the reaction intermediates, which could work with the Cu sites to trigger the C-C coupling in order to produce the C_2 products (*e.g.*, C_2H_4 and C_2H_6).

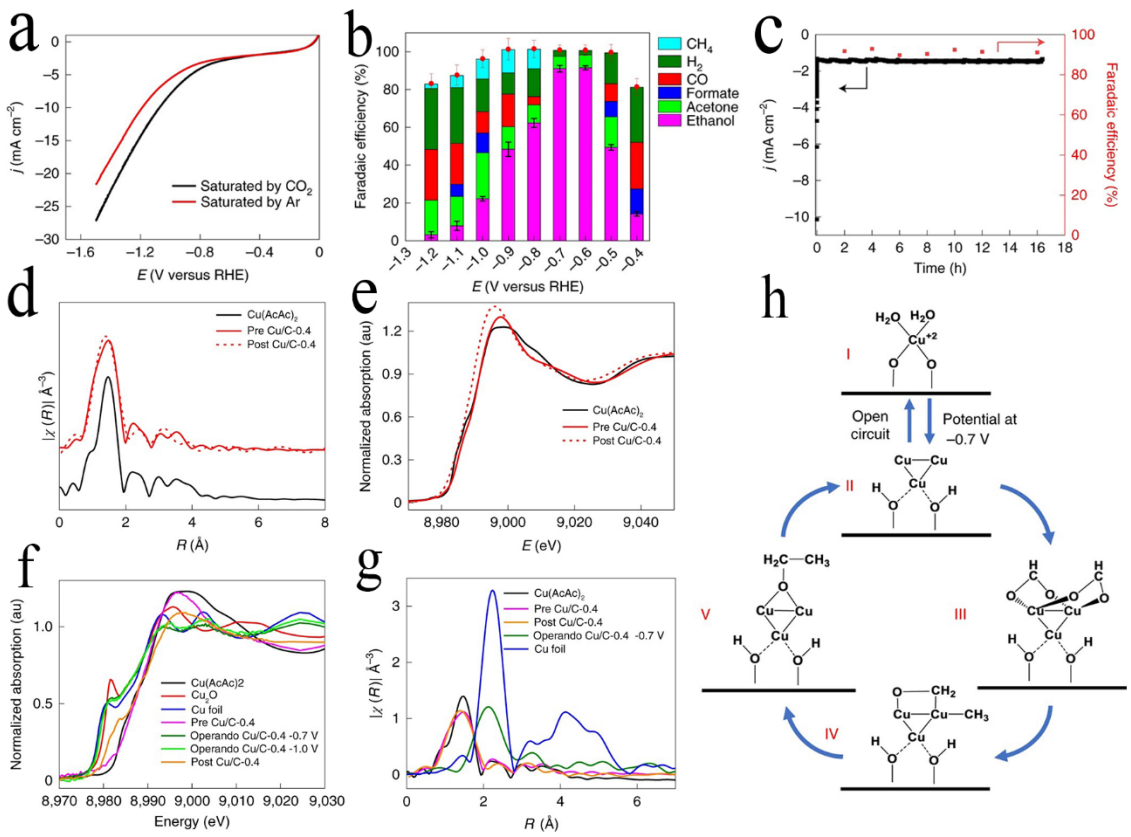

Figure 12. (a) LSV curves of Cu/C-0.4 (0.4 wt% Cu loading) in Ar and CO_2 saturated 0.1 M $KHCO_3$ at a scan rate of 50 mV s^{-1}. (b) The FE for all detected products at different reduction potentials. (c) The ethanol FE and current density as a function of operation time at –0.6 V. (d) Fourier transform of EXAFS data and (e) Cu K-edge normalized XANES spectra for Cu/C-0.4 before and after 16 hours testing. (f) In situ Cu XANES spectra and (g) corresponding Fourier transform spectra for Cu/C-0.4 at different reduction potentials. (f) The hypothesized reaction mechanism is based on operando measurements. Reproduced with permission.[109] Copyright 2020, Nature Publishing Group.

6. Summary and Outlook

This review summarized the recent progress in synthesizing different types of carbon-supported SACs for application in electrocatalytic CO_2RR, including the MN_x catalysts, heterogeneous molecular catalysts, and COF based SACs. Although the vigorous development of carbon-supported SACs in other energy-related electrochemical reactions could provide guidance in preparation and characterization methods, the electrochemical CO_2 reduction using carbon-supported SACs is still in its infancy. Due to the complicated intermediates and reaction pathways for the CO_2RR, the catalytic selectivity is an important parameter that needs to be considered. By rationally choosing the metal centers and modulating their electronic structure, many carbon-supported SACs have exhibited outstanding CO_2RR performance with high selectivity for CO production. However, the selectivity of carbon-supported SACs for other high-value multielectron products is far from satisfactory for practical applications. A large amount of experimental data has revealed the metal centers' CO2RR performance is not merely related to the local coordination environment but also the long-range electronic intercalation from the carbon substrates. Fully understanding the metal-substrate interactions is incredibly significant for the rational design of highly active and selective SACs. Also, the choice of MN_x based catalysts has several advantages, such as densely dispersed active sites, good conductivity, and fast mass transfer. However, optimizing their performance is still primarily at the mercy of trial-and-error approaches because of a lack of controllable synthesis methods. Therefore, elucidating the reaction mechanism of CO_2RR on the carbon-supported SACs is essential to perform optimizations on reaction conditions and the structures of catalysts. The heterogeneous molecular catalysts and COF based catalysts offer an alternative way to realize theory-guided catalyst preparation due to their uniform structure and well-defined active sites. However, the intuitive and accurate descriptors that correlate the

CO_2RR activity with the electronic structures of the SACs are still needed to screen the suitable metal centers and corresponding configurations quickly.

More effort should be devoted to examining the structure-activity relationship by using advanced characterization technologies of atomic-level resolution and more accurate theoretical calculations. Many characterizations are currently carried out in ex-situ conditions, which cannot reflect the real state of SACs sites during the CO_2RR process, providing incorrect information for theoretical modeling. Monitoring atomic and electronic structure changes of SACs under realistic working conditions based on in-situ technologies, such as in-situ FT-IR, Raman, and XAS characterizations, are crucial for better understanding of the active centers and reaction mechanisms, thus paving the way for the more rational design of efficient CO_2RR electrocatalysts.

Generating C_2 products is of great significance for CO_2 reduction. However, in principle, it is difficult to simultaneously activate two CO_2 molecules to trigger the C-C coupling reaction based on an isolated metal center. Developing novel dual metal sites or utilizing the heteroatoms' synergistic effect might be effective ways to solve the single metal sites' intrinsic limitation. Also, the development of the self-support binder-free gas diffusion electrode and flow reactors are necessary for practical applications of CO_2 reduction. Such a reaction condition weakened CO2 diffusion's influence compared to typical H-type cells, leading to different reduction mechanisms and CO_2RR performance. Therefore, further study is required to optimize the operating conditions and the macrostructure and mesostructure of the electrode to integrate SACs into flow cells effectively.

Acknowledgments

G.W. acknowledges the National Science Foundation (CBET-1804326). Y.Z. acknowledges the National Natural Science Foundation of China (No. 21908088).

Received: ((will be filled in by the editorial staff))
Revised: ((will be filled in by the editorial staff))
Published online: ((will be filled in by the editorial staff))

References

[1] a) P. De Luna, C. Hahn, D. Higgins, S. A. Jaffer, T. F. Jaramillo, E. H. Sargent, *Science* **2019**, *364*, eaav3506; b) N. Bauer, I. Mouratiadou, G. Luderer, L. Baumstark, R. J. Brecha, O. Edenhofer, E. Kriegler, *Climatic Change* **2013**, *136*, 69-82.

[2] S. Nitopi, E. Bertheussen, S. B. Scott, X. Liu, A. K. Engstfeld, S. Horch, B. Seger, I. E. L. Stephens, K. Chan, C. Hahn, J. K. Norskov, T. F. Jaramillo, I. Chorkendorff, *Chem Rev* **2019**, *119*, 7610-7672.

[3] a) X. Wang, Q. Zhao, B. Yang, Z. Li, Z. Bo, K. H. Lam, N. M. Adli, L. Lei, Z. Wen, G. Wu, Y. Hou, *Journal of Materials Chemistry A* **2019**, *7*, 25191-25202; b) J. Qiao, Y. Liu, F. Hong, J. Zhang, *Chem Soc Rev* **2014**, *43*, 631-675; c) L. Wang, W. Chen, D. Zhang, Y. Du, R. Amal, S. Qiao, J. Wu, Z. Yin, *Chem Soc Rev* **2019**, *48*, 5310-5349.

[4] R. Daiyan, W. H. Saputera, H. Masood, J. Leverett, X. Lu, R. Amal, *Advanced Energy Materials* **2020**, *10*, 1902106.

[5] a) S. Liu, M. Wang, X. Yang, Q. Shi, Z. Qiao, M. Lucero, Q. Ma, K. L. More, D. A. Cullen, Z. Feng, G. Wu, *Angewandte Chemie International Edition* **2020**, *n/a*; b) X. Zhao, X. Yang, M. Wang, S. Hwang, S. Karakalos, M. Chen, Z. Qiao, L. Wang, B. Liu, Q. Ma, D. A. Cullen, D. Su, H. Yang, H.-Y. Zang, Z. Feng, G. Wu, *Applied Catalysis B: Environmental* **2020**, *279*, 119400; c) Y. He, S. Liu, C. Priest, Q. Shi, G. Wu, *Chemical Society Reviews* **2020**, *49*, 3484-3524; d) Y. Li, H. Wang, C. Priest, S. Li, P. Xu, G. Wu, *Advanced Materials* **2020**, *n/a*, 2000381; e) J. Li, H. Zhang, W. Samarakoon, W. Shan, D. A. Cullen, S. Karakalos, M. Chen, D. Gu, K. L. More, G. Wang, Z. Feng, Z. Wang, G. Wu, *Angew Chem Int Ed Engl* **2019**, *58*, 18971-18980; f) Q. Shi, Y. He, X. Bai, M. Wang, D. A. Cullen, M. Lucero, X. Zhao, K. L. More, H. Zhou, Z. Feng, Y. Liu, G. Wu, *Energy & Environmental Science* **2020**; g) X. X. Wang, M. T. Swihart, G. Wu, *Nature Catalysis* **2019**, *2*, 578-589; h) J. Li, M. Chen, D. A. Cullen, S. Hwang, M. Wang, B. Li, K. Liu, S.

Karakalos, M. Lucero, H. Zhang, C. Lei, H. Xu, G. E. Sterbinsky, Z. Feng, D. Su, K. L. More, G. Wang, Z. Wang, G. Wu, *Nature Catalysis* **2018**, *1*, 935-945; i) Y. He, S. Hwang, D. A. Cullen, M. A. Uddin, L. Langhorst, B. Li, S. Karakalos, A. J. Kropf, E. C. Wegener, J. Sokolowski, M. Chen, D. Myers, D. Su, K. L. More, G. Wang, S. Litster, G. Wu, *Energy & Environmental Science* **2019**, *12*, 250-260; j) X. X. Wang, D. A. Cullen, Y.-T. Pan, S. Hwang, M. Wang, Z. Feng, J. Wang, M. H. Engelhard, H. Zhang, Y. He, Y. Shao, D. Su, K. L. More, J. S. Spendelow, G. Wu, *Advanced Materials* **2018**, *30*, 1706758.

[6] a) S. Mukherjee, X. Yang, W. Shan, W. Samarakoon, S. Karakalos, D. A. Cullen, K. More, M. Wang, Z. Feng, G. Wang, G. Wu, *Small Methods* **2020**, *4*, 1900821; b) S. Mukherjee, D. A. Cullen, S. Karakalos, K. Liu, H. Zhang, S. Zhao, H. Xu, K. L. More, G. Wang, G. Wu, *Nano Energy* **2018**, *48*, 217-226; c) H. Xu, K. Ithisuphalap, Y. Li, S. Mukherjee, J. Lattimer, G. Soloveichik, G. Wu, *Nano Energy* **2020**, *69*, 104469.

[7] a) C. Zhu, S. Fu, Q. Shi, D. Du, Y. Lin, *Angew Chem Int Ed Engl* **2017**, *56*, 13944-13960; b) B. Bayatsarmadi, Y. Zheng, A. Vasileff, S. Z. Qiao, *Small* **2017**, *13*, 1700191.

[8] X. Wang, Z. Chen, X. Zhao, T. Yao, W. Chen, R. You, C. Zhao, G. Wu, J. Wang, W. Huang, J. Yang, X. Hong, S. Wei, Y. Wu, Y. Li, *Angewandte Chemie* **2018**, *130*, 1962-1966.

[9] J. Gu, C. S. Hsu, L. Bai, H. M. Chen, X. Hu, *Science* **2019**, *364*, 1091-1094.

[10] H. Zhang, J. Li, S. Xi, Y. Du, X. Hai, J. Wang, H. Xu, G. Wu, J. Zhang, J. Lu, J. Wang, *Angewandte Chemie* **2019**, *131*, 15013-15018.

[11] X. Rong, H. J. Wang, X. L. Lu, R. Si, T. B. Lu, *Angew Chem Int Ed Engl* **2020**, *59*, 1961-1965.

[12] X. Zu, X. Li, W. Liu, Y. Sun, J. Xu, T. Yao, W. Yan, S. Gao, C. Wang, S. Wei, Y. Xie, *Adv Mater* **2019**, *31*, e1808135.

[13] a) Y. Wu, Z. Jiang, X. Lu, Y. Liang, H. Wang, *Nature* **2019**, *575*, 639-642; b) H. Yang, Y. Wu, G. Li, Q. Lin, Q. Hu, Q. Zhang, J. Liu, C. He, *J Am Chem Soc* **2019**, *141*, 12717-12723.

[14] L. Han, S. Song, M. Liu, S. Yao, Z. Liang, H. Cheng, Z. Ren, W. Liu, R. Lin, G. Qi, X. Liu, Q. Wu, J. Luo, H. L. Xin, *J Am Chem Soc* **2020**, *142*, 12563-12567.

[15] D. Karapinar, N. T. Huan, N. Ranjbar Sahraie, J. Li, D. Wakerley, N. Touati, S. Zanna, D. Taverna, L. H. Galvao Tizei, A. Zitolo, F. Jaouen, V. Mougel, M. Fontecave, *Angew Chem Int Ed Engl* **2019**, *58*, 15098-15103.

[16] A. Guan, Z. Chen, Y. Quan, C. Peng, Z. Wang, T.-K. Sham, C. Yang, Y. Ji, L. Qian, X. Xu, G. Zheng, *ACS Energy Letters* **2020**, *5*, 1044-1053.

[17] Y. Jiao, Y. Zheng, P. Chen, M. Jaroniec, S. Z. Qiao, *J Am Chem Soc* **2017**, *139*, 18093-18100.

[18] K. Jiang, S. Siahrostami, A. J. Akey, Y. Li, Z. Lu, J. Lattimer, Y. Hu, C. Stokes, M. Gangishetty, G. Chen, Y. Zhou, W. Hill, W.-B. Cai, D. Bell, K. Chan, J. K. Nørskov, Y. Cui, H. Wang, *Chem* **2017**, *3*, 950-960.

[19] J. Tuo, Y. Lin, Y. Zhu, H. Jiang, Y. Li, L. Cheng, R. Pang, J. Shen, L. Song, C. Li, *Applied Catalysis B: Environmental* **2020**, *272*, 118960.

[20] H. J. Zhu, M. Lu, Y. R. Wang, S. J. Yao, M. Zhang, Y. H. Kan, J. Liu, Y. Chen, S. L. Li, Y. Q. Lan, *Nat Commun* **2020**, *11*, 497.

[21] C. Yan, H. Li, Y. Ye, H. Wu, F. Cai, R. Si, J. Xiao, S. Miao, S. Xie, F. Yang, Y. Li, G. Wang, X. Bao, *Energy & Environmental Science* **2018**, *11*, 1204-1210.

[22] a) F. Pan, H. Zhang, K. Liu, D. Cullen, K. More, M. Wang, Z. Feng, G. Wang, G. Wu, Y. Li, *ACS Catalysis* **2018**, *8*, 3116-3122; b) F. Pan, H. Zhang, Z. Liu, D. Cullen, K. Liu, K. More, G. Wu, G. Wang, Y. Li, *Journal of Materials Chemistry A* **2019**, *7*, 26231-26237.

[23] J. Guo, Y. Li, Y. Cheng, L. Dai, Z. Xiang, *ACS Nano* **2017**, *11*, 8379-8386.

[24] a) C. Xu, A. Vasileff, D. Wang, B. Jin, Y. Zheng, S.-Z. Qiao, *Nanoscale Horizons* **2019**, *4*, 1411-1415; b) C. Lei, Y. Wang, Y. Hou, P. Liu, J. Yang, T. Zhang, X. Zhuang, M. Chen, B. Yang, L. Lei, C. Yuan, M. Qiu, X. Feng, *Energy & Environmental Science* **2019**, *12*, 149-156.

[25] W. Ju, A. Bagger, G. P. Hao, A. S. Varela, I. Sinev, V. Bon, B. Roldan Cuenya, S. Kaskel, J. Rossmeisl, P. Strasser, *Nat Commun* **2017**, *8*, 944.

[26] D. M. Koshy, S. Chen, D. U. Lee, M. B. Stevens, A. M. Abdellah, S. M. Dull, G. Chen, D. Nordlund, A. Gallo, C. Hahn, D. C. Higgins, Z. Bao, T. F. Jaramillo, *Angewandte Chemie* **2020**, *132*, 4072-4079.

[27] R. Francke, B. Schille, M. Roemelt, *Chem Rev* **2018**, *118*, 4631-4701.

[28] a) J. Wang, X. Huang, S. Xi, J. M. Lee, C. Wang, Y. Du, X. Wang, *Angew Chem Int Ed Engl* **2019**, *58*, 13532-13539; b) M. Zhu, J. Chen, L. Huang, R. Ye, J. Xu, Y. F. Han, *Angew Chem Int Ed Engl* **2019**, *58*, 6595-6599.

[29] X. Zhang, Z. Wu, X. Zhang, L. Li, Y. Li, H. Xu, X. Li, X. Yu, Z. Zhang, Y. Liang, H. Wang, *Nat Commun* **2017**, *8*, 14675.

[30] S. Liu, H. B. Yang, S. F. Hung, J. Ding, W. Cai, L. Liu, J. Gao, X. Li, X. Ren, Z. Kuang, Y. Huang, T. Zhang, B. Liu, *Angew Chem Int Ed Engl* **2020**, *59*, 798-803.

[31] a) Y. Yoon, A. S. Hall, Y. Surendranath, *Angew Chem Int Ed Engl* **2016**, *55*, 15282-15286; b) A. S. Hall, Y. Yoon, A. Wuttig, Y. Surendranath, *J Am Chem Soc* **2015**, *137*, 14834-14837.

[32] J. Wang, L. Gan, Q. Zhang, V. Reddu, Y. Peng, Z. Liu, X. Xia, C. Wang, X. Wang, *Advanced Energy Materials* **2019**, *9*, 1803151.

[33] M. Zhu, R. Ye, K. Jin, N. Lazouski, K. Manthiram, *ACS Energy Letters* **2018**, *3*, 1381-1386.

[34] S. A. Yao, R. E. Ruther, L. Zhang, R. A. Franking, R. J. Hamers, J. F. Berry, *J Am Chem Soc* **2012**, *134*, 15632-15635.

[35] a) S. Lin, C. S. Diercks, Y. B. Zhang, N. Kornienko, E. M. Nichols, Y. Zhao, A. R. Paris, D. Kim, P. Yang, O. M. Yaghi, C. J. Chang, *Science* **2015**, *349*, 1208-1213; b) Q. Wu, R.-K. Xie, M.-J. Mao, G.-L. Chai, J.-D. Yi, S.-S. Zhao, Y.-B. Huang, R. Cao, *ACS Energy Letters* **2020**, *5*, 1005-1012.

[36] a) P. T. Smith, B. P. Benke, Z. Cao, Y. Kim, E. M. Nichols, K. Kim, C. J. Chang, *Angew Chem Int Ed Engl* **2018**, *57*, 9684-9688; b) Y. Hou, Y.-B. Huang, Y.-L. Liang, G.-L. Chai, J.-D. Yi, T. Zhang, K.-T. Zang, J. Luo, R. Xu, H. Lin, S.-Y. Zhang, H.-M. Wang, R. Cao, *CCS Chemistry* **2019**, *1*, 384-395.

[37] a) P. Su, K. Iwase, T. Harada, K. Kamiya, S. Nakanishi, *Chem Sci* **2018**, *9*, 3941-3947; b) L. Ma, W. Hu, B. Mei, H. Liu, B. Yuan, J. Zang, T. Chen, L. Zou, Z. Zou, B. Yang, Y. Yu, J. Ma, Z. Jiang, K. Wen, H. Yang, *ACS Catalysis* **2020**, *10*, 4534-4542; c) S. Feng, W. Zheng, J. Zhu, Z. Li, B. Yang, Z. Wen, J. Lu, L. Lei, S. Wang, Y. Hou, *Applied Catalysis B: Environmental* **2020**, *270*.

[38] a) J. Chen, Z. Wang, H. Lee, J. Mao, C. A. Grimes, C. Liu, M. Zhang, Z. Lu, Y. Chen, S. P. Feng, *Materials Today Physics* **2020**, *12*, 100176; b) C. Ao, B. Feng, S. Qian, L. Wang, W. Zhao, Y. Zhai, L. Zhang, *Journal of CO_2 Utilization* **2020**, *36*, 116-123.

[39] a) H. Shen, Q. Sun, *The Journal of Physical Chemistry C* **2019**, *123*, 29776-29782; b) X. Liu, Z. Wang, Y. Tian, J. Zhao, *The Journal of Physical Chemistry C* **2020**, *124*, 3722-3730.

[40] Y. Ye, F. Cai, H. Li, H. Wu, G. Wang, Y. Li, S. Miao, S. Xie, R. Si, J. Wang, X. Bao, *Nano Energy* **2017**, *38*, 281-289.

[41] C. Zhao, X. Dai, T. Yao, W. Chen, X. Wang, J. Wang, J. Yang, S. Wei, Y. Wu, Y. Li, *J Am Chem Soc* **2017**, *139*, 8078-8081.

[42] W. Ren, X. Tan, W. Yang, C. Jia, S. Xu, K. Wang, S. C. Smith, C. Zhao, *Angew Chem Int Ed Engl* **2019**, *58*, 6972-6976.

[43] F. Wang, H. Xie, T. Liu, Y. Wu, B. Chen, *Applied Energy* **2020**, *269*.

[44] T. Wang, X. Sang, W. Zheng, B. Yang, S. Yao, C. Lei, Z. Li, Q. He, J. Lu, L. Lei, L. Dai, Y. Hou, *Adv Mater* **2020**, e2002430.

[45] C. Zhang, Z. Fu, Q. Zhao, Z. Du, R. Zhang, S. Li, *Electrochemistry Communications* **2020**, *116*, 106758.

[46] P. Su, K. Iwase, S. Nakanishi, K. Hashimoto, K. Kamiya, *Small* **2016**, *12*, 6083-6089.

[47] a) C. Zhang, S. Yang, J. Wu, M. Liu, S. Yazdi, M. Ren, J. Sha, J. Zhong, K. Nie, A. S. Jalilov, Z. Li, H. Li, B. I. Yakobson, Q. Wu, E. Ringe, H. Xu, P. M. Ajayan, J. M. Tour, *Advanced Energy Materials* **2018**, *8*, 1703487; b) K. Jiang, S. Siahrostami, T. Zheng, Y. Hu, S. Hwang, E. Stavitski, Y. Peng, J. Dynes, M. Gangisetty, D. Su, K. Attenkofer, H. Wang, *Energy & Environmental Science* **2018**, *11*, 893-903.

[48] Q. Fan, P. Hou, C. Choi, T. S. Wu, S. Hong, F. Li, Y. L. Soo, P. Kang, Y. Jung, Z. Sun, *Advanced Energy Materials* **2019**, *10*, 1903068.

[49] Y. Cheng, S. Zhao, B. Johannessen, J. P. Veder, M. Saunders, M. R. Rowles, M. Cheng, C. Liu, M. F. Chisholm, R. De Marco, H. M. Cheng, S. Z. Yang, S. P. Jiang, *Adv Mater* **2018**, *30*, e1706287.

[50] H. B. Yang, S.-F. Hung, S. Liu, K. Yuan, S. Miao, L. Zhang, X. Huang, H.-Y. Wang, W. Cai, R. Chen, J. Gao, X. Yang, W. Chen, Y. Huang, H. M. Chen, C. M. Li, T. Zhang, B. Liu, *Nature Energy* **2018**, *3*, 140-147.

[51] Y. N. Gong, L. Jiao, Y. Qian, C. Y. Pan, L. Zheng, X. Cai, B. Liu, S. H. Yu, H. L. Jiang, *Angewandte Chemie International Edition* **2020**, *59*, 2705-2709.

[52] W. Zheng, J. Yang, H. Chen, Y. Hou, Q. Wang, M. Gu, F. He, Y. Xia, Z. Xia, Z. Li, B. Yang, L. Lei, C. Yuan, Q. He, M. Qiu, X. Feng, *Advanced Functional Materials* **2019**, *30*, 1907658.

[53] F. Yang, P. Song, X. Liu, B. Mei, W. Xing, Z. Jiang, L. Gu, W. Xu, *Angew Chem Int Ed Engl* **2018**, *57*, 12303-12307.

[54] J. Li, L. Jiao, E. Wegener, L. L. Richard, E. Liu, A. Zitolo, M. T. Sougrati, S. Mukerjee, Z. Zhao, Y. Huang, F. Yang, S. Zhong, H. Xu, A. J. Kropf, F. Jaouen, D. J. Myers, Q. Jia, *J Am Chem Soc* **2020**, *142*, 1417-1423.

[55] a) X. Sun, R. Wang, S. Ould-Chikh, D. Osadchii, G. Li, A. Aguilar, J.-l. Hazemann, F. Kapteijn, J. Gascon, *Journal of Catalysis* **2019**, *378*, 320-330; b) S. Ma, P. Su, W. Huang, S. P. Jiang, S. Bai, J. Liu, *ChemCatChem* **2019**, *11*, 6092-6098; c) W. Kou, Y. Zhang, J. Dong, C. Mu, L. Xu, *ACS Applied Energy Materials* **2020**, *3*, 1875-1882.

[56] X. Wang, Y. Pan, H. Ning, H. Wang, D. Guo, W. Wang, Z. Yang, Q. Zhao, B. Zhang, L. Zheng, J. Zhang, M. Wu, *Applied Catalysis B: Environmental* **2020**, *266*, 118630.

[57] Z. Guo, N. Xiao, H. Li, Y. Wang, C. Li, C. Liu, J. Xiao, J. Bai, S. Zhao, J. Qiu, *Journal of CO_2 Utilization* **2020**, *38*, 212-219.

[58] J.-J. Shi, X.-M. Hu, M. R. Madsen, P. Lamagni, E. T. Bjerglund, S. U. Pedersen, T. Skrydstrup, K. Daasbjerg, *ACS Applied Nano Materials* **2018**, *1*, 3608-3615.

[59] Y. Hou, Y.-L. Liang, P.-C. Shi, Y.-B. Huang, R. Cao, *Applied Catalysis B: Environmental* **2020**, *271*, 118929.

[60] a) J. Wang, Z. Huang, W. Liu, C. Chang, H. Tang, Z. Li, W. Chen, C. Jia, T. Yao, S. Wei, Y. Wu, Y. Li, *J Am Chem Soc* **2017**, *139*, 17281-17284; b) X. Chen, D.-D. Ma, B. Chen, K. Zhang, R. Zou, X.-T. Wu, Q.-L. Zhu, *Applied Catalysis B: Environmental* **2020**, *267*, 118720.

[61] E. Zhang, T. Wang, K. Yu, J. Liu, W. Chen, A. Li, H. Rong, R. Lin, S. Ji, X. Zheng, Y. Wang, L. Zheng, C. Chen, D. Wang, J. Zhang, Y. Li, *J Am Chem Soc* **2019**, *141*, 16569-16573.

[62] a) C. Zhang, Y. C. Wang, B. An, R. Huang, C. Wang, Z. Zhou, W. Lin, *Adv Mater* **2017**, *29*, 1604556; b) G. Wu, N. H. Mack, W. Gao, S. Ma, R. Zhong, J. Han, J. K. Baldwin, P. Zelenay, *ACS Nano* **2012**, *6*, 9764-9776.

[63] F. Pan, B. Li, E. Sarnello, Y. Fei, Y. Gang, X. Xiang, Z. Du, P. Zhang, G. Wang, H. T. Nguyen, T. Li, Y. H. Hu, H. C. Zhou, Y. Li, *ACS Nano* **2020**, *14*, 5506-5516.

[64] H. Yang, Q. Lin, C. Zhang, X. Yu, Z. Cheng, G. Li, Q. Hu, X. Ren, Q. Zhang, J. Liu, C. He, *Nat Commun* **2020**, *11*, 593.

[65] a) A. Maurin, M. Robert, *J Am Chem Soc* **2016**, *138*, 2492-2495; b) S. Aoi, K. Mase, K. Ohkubo, S. Fukuzumi, *Chem Commun (Camb)* **2015**, *51*, 10226-10228.

[66] a) N. Morlanés, K. Takanabe, V. Rodionov, *ACS Catalysis* **2016**, *6*, 3092-3095; b) J. Choi, P. Wagner, S. Gambhir, R. Jalili, D. R. MacFarlane, G. G. Wallace, D. L. Officer, *ACS Energy Letters* **2019**, *4*, 666-672; c) M. Wang, K. Torbensen, D. Salvatore, S. Ren, D. Joulie, F. Dumoulin, D. Mendoza, B. Lassalle-Kaiser, U. Isci, C. P. Berlinguette, M. Robert, *Nat Commun* **2019**, *10*, 3602.

[67] a) N. Elgrishi, M. B. Chambers, X. Wang, M. Fontecave, *Chem Soc Rev* **2017**, *46*, 761-796; b) B. Reuillard, K. H. Ly, T. E. Rosser, M. F. Kuehnel, I. Zebger, E. Reisner, *J Am Chem Soc* **2017**, *139*, 14425-14435.

[68] X. M. Hu, M. H. Ronne, S. U. Pedersen, T. Skrydstrup, K. Daasbjerg, *Angew Chem Int Ed Engl* **2017**, *56*, 6468-6472.

[69] P. Kang, S. Zhang, T. J. Meyer, M. Brookhart, *Angew Chem Int Ed Engl* **2014**, *53*, 8709-8713.

[70] J. Choi, J. Kim, P. Wagner, S. Gambhir, R. Jalili, S. Byun, S. Sayyar, Y. M. Lee, D. R. MacFarlane, G. G. Wallace, D. L. Officer, *Energy & Environmental Science* **2019**, *12*, 747-755.

[71] J. Li, P. Pršlja, T. Shinagawa, A. J. Martín Fernández, F. Krumeich, K. Artyushkova, P. Atanassov, A. Zitolo, Y. Zhou, R. García-Muelas, N. López, J. Pérez-Ramírez, F. Jaouen, *ACS Catalysis* **2019**, *9*, 10426-10439.

[72] Y. Chen, Y. Yao, Y. Xia, K. Mao, G. Tang, Q. Wu, L. Yang, X. Wang, X. Sun, Z. Hu, *Nano Research* **2020**, *13*, 2777-2783.

[73] T. Zhang, X. Han, H. Yang, A. Han, E. Hu, Y. Li, X. Q. Yang, L. Wang, J. Liu, B. Liu, *Angew Chem Int Ed Engl* **2020**, *59*, 12055-12061.

[74] X. Wang, D. Wu, C. Dai, C. Xu, P. Sui, R. Feng, Y. Wei, X.-Z. Fu, J.-L. Luo, *Journal of Materials Chemistry A* **2020**, *8*, 5105-5114.

[75] J. Deng, P. Ren, D. Deng, X. Bao, *Angew Chem Int Ed Engl* **2015**, *54*, 2100-2104.

[76] T. Zheng, K. Jiang, N. Ta, Y. Hu, J. Zeng, J. Liu, H. Wang, *Joule* **2019**, *3*, 265-278.

[77] T. Möller, W. Ju, A. Bagger, X. Wang, F. Luo, T. Ngo Thanh, A. S. Varela, J. Rossmeisl, P. Strasser, *Energy & Environmental Science* **2019**, *12*, 640-647.

[78] A. S. Varela, N. Ranjbar Sahraie, J. Steinberg, W. Ju, H.-S. Oh, P. Strasser, *Angewandte Chemie* **2015**, *127*, 10908-10912.

[79] a) F. Pan, W. Deng, C. Justiniano, Y. Li, *Applied Catalysis B: Environmental* **2018**, *226*, 463-472; b) T. N. Huan, N. Ranjbar, G. Rousse, M. Sougrati, A. Zitolo, V. Mougel, F. Jaouen, M. Fontecave, *ACS Catalysis* **2017**, *7*, 1520-1525; c) X.-M. Hu, H. H. Hval, E. T. Bjerglund, K. J. Dalgaard, M. R. Madsen, M.-M. Pohl, E. Welter, P. Lamagni, K. B. Buhl, M. Bremholm, M. Beller, S. U. Pedersen, T. Skrydstrup, K. Daasbjerg, *ACS Catalysis* **2018**, *8*, 6255-6264.

[80] T. Asset, S. T. Garcia, S. Herrera, N. Andersen, Y. Chen, E. J. Peterson, I. Matanovic, K. Artyushkova, J. Lee, S. D. Minteer, S. Dai, X. Pan, K. Chavan, S. Calabrese Barton, P. Atanassov, *ACS Catalysis* **2019**, *9*, 7668-7678.

[81] Y. Wang, M. Wang, Z. Zhang, Q. Wang, Z. Jiang, M. Lucero, X. Zhang, X. Li, M. Gu, Z. Feng, Y. Liang, *ACS Catalysis* **2019**, *9*, 6252-6261.

[82] F. Pan, B. Li, E. Sarnello, S. Hwang, Y. Gang, X. Feng, X. Xiang, N. M. Adli, T. Li, D. Su, G. Wu, G. Wang, Y. Li, *Nano Energy* **2020**, *68*.

[83] N. Mohd Adli, W. Shan, S. Hwang, W. Samarakoon, S. Karakalos, Y. Li, D. A. Cullen, D. Su, Z. Feng, G. Wang, G. Wu, *Angewandte Chemie International Edition* **2020**, *n/a*.

[84] X. Qin, S. Zhu, F. Xiao, L. Zhang, M. Shao, *ACS Energy Letters* **2019**, *4*, 1778-1783.

[85] aR. Shang, S. N. Steinmann, B.-Q. Xu, P. Sautet, *Catalysis Science & Technology* **2020**, *10*, 1006-1014; bX. Zhao, X. Liu, B. Huang, P. Wang, Y. Pei, *Journal of Materials Chemistry A* **2019**, *7*, 24583-24593.

[86] Y. Zhu, X. Li, X. Wang, K. Lv, G. Xiao, J. Feng, X. Jiang, M. Fang, Y. Zhu, *ChemistrySelect* **2020**, *5*, 1282-1287.

[87] Z. Geng, Y. Cao, W. Chen, X. Kong, Y. Liu, T. Yao, Y. Lin, *Applied Catalysis B: Environmental* **2019**, *240*, 234-240.

[88] S. Dou, X. Wang, S. Wang, *Small Methods* **2019**, *3*.

[89] H. Yang, Q. Lin, Y. Wu, G. Li, Q. Hu, X. Chai, X. Ren, Q. Zhang, J. Liu, C. He, *Nano Energy* **2020**, *70*, 104454.

[90] X. Chen, X.-M. Hu, K. Daasbjerg, M. S. G. Ahlquist, *Organometallics* **2020**, *39*, 1634-1641.

[91] G. Zhu, Y. Li, H. Zhu, H. Su, S. H. Chan, Q. Sun, *ACS Catalysis* **2016**, *6*, 6294-6301.

[92] L. Sun, Z. Huang, V. Reddu, T. Su, A. C. Fisher, X. Wang, *Angew Chem Int Ed Engl* **2020**.

[93] Y. Pan, R. Lin, Y. Chen, S. Liu, W. Zhu, X. Cao, W. Chen, K. Wu, W.-C. Cheong, Y. Wang, L. Zheng, J. Luo, Y. Lin, Y. Liu, C. Liu, J. Li, Q. Lu, X. Chen, D. Wang, Q. Peng, C. Chen, Y. Li, *Journal of the American Chemical Society* **2018**, *140*, 4218-4221.

[94] Z. Chen, K. Mou, S. Yao, L. Liu, *ChemSusChem* **2018**, *11*, 2944-2952.

[95] J. Feng, H. Gao, L. Zheng, Z. Chen, S. Zeng, C. Jiang, H. Dong, L. Liu, S. Zhang, X. Zhang, *Nature Communications* **2020**, *11*, 4341.

[96] B. Zhang, J. Zhang, J. Shi, D. Tan, L. Liu, F. Zhang, C. Lu, Z. Su, X. Tan, X. Cheng, B. Han, L. Zheng, J. Zhang, *Nat Commun* **2019**, *10*, 2980.

[97] a) S. Oh, J. R. Gallagher, J. T. Miller, Y. Surendranath, *J Am Chem Soc* **2016**, *138*, 1820-1823; b) A. Zhanaidarova, S. C. Jones, E. Despagnet-Ayoub, B. R. Pimentel, C. P. Kubiak, *J Am Chem Soc* **2019**, *141*, 17270-17277.

[98] M. N. Jackson, S. Oh, C. J. Kaminsky, S. B. Chu, G. Zhang, J. T. Miller, Y. Surendranath, *J Am Chem Soc* **2018**, *140*, 1004-1010.

[99] T. He, L. Zhang, G. Kour, A. Du, *Journal of CO2 Utilization* **2020**, *37*, 272-277.

[100] S. Chen, H. Yuan, S. I. Morozov, L. Ge, L. Li, L. Xu, W. A. Goddard, *The Journal of Physical Chemistry Letters* **2020**, *11*, 2541-2549.

[101] Q. Huang, H. Liu, W. An, Y. Wang, Y. Feng, Y. Men, *ACS Sustainable Chemistry & Engineering* **2019**, *7*, 19113-19121.

[102] W. Zhu, L. Zhang, S. Liu, A. Li, X. Yuan, C. Hu, G. Zhang, W. Deng, K. Zang, J. Luo, Y. Zhu, M. Gu, Z. J. Zhao, J. Gong, *Angewandte Chemie International Edition* **2020**, *59*, 12664-12668.

[103] P. Huang, M. Cheng, H. Zhang, M. Zuo, C. Xiao, Y. Xie, *Nano Energy* **2019**, *61*, 428-434.

[104] H. Shang, T. Wang, J. Pei, Z. Jiang, D. Zhou, Y. Wang, H. Li, J. Dong, Z. Zhuang, W. Chen, D. Wang, J. Zhang, Y. Li, *Angew Chem Int Ed Engl* **2020**, https://doi.org/10.1002/anie.202010903.

[105] J. Shen, R. Kortlever, R. Kas, Y. Y. Birdja, O. Diaz-Morales, Y. Kwon, I. Ledezma-Yanez, K. J. Schouten, G. Mul, M. T. Koper, *Nat Commun* **2015**, *6*, 8177.

[106] a) W. Ju, A. Bagger, X. Wang, Y. Tsai, F. Luo, T. Möller, H. Wang, J. Rossmeisl, A. S. Varela, P. Strasser, *ACS Energy Letters* **2019**, *4*, 1663-1671; b) A. S. Varela, M. Kroschel, N. D. Leonard, W. Ju, J. Steinberg, A. Bagger, J. Rossmeisl, P. Strasser, *ACS Energy Letters* **2018**, *3*, 812-817.

[107] a) Z. Weng, Y. Wu, M. Wang, J. Jiang, K. Yang, S. Huo, X. F. Wang, Q. Ma, G. W. Brudvig, V. S. Batista, Y. Liang, Z. Feng, H. Wang, *Nat Commun* **2018**, *9*, 415; b) Z. Weng, J. Jiang, Y. Wu, Z. Wu, X. Guo, K. L. Materna, W. Liu, V. S. Batista, G. W. Brudvig, H. Wang, *J Am Chem Soc* **2016**, *138*, 8076-8079.

[108] N. Leonard, W. Ju, I. Sinev, J. Steinberg, F. Luo, A. S. Varela, B. Roldan Cuenya, P. Strasser, *Chem Sci* **2018**, *9*, 5064-5073.

[109] H. Xu, D. Rebollar, H. He, L. Chong, Y. Liu, C. Liu, C.-J. Sun, T. Li, J. V. Muntean, R. E. Winans, D.-J. Liu, T. Xu, *Nature Energy* **2020**, *10.1038/s41560-020-0666-x*.

[110] a) M. Balamurugan, H. Y. Jeong, V. S. K. Choutipalli, J. S. Hong, H. Seo, N. Saravanan, J. H. Jang, K. G. Lee, Y. H. Lee, S. W. Im, V. Subramanian, S. H. Kim, K. T. Nam, *Small* **2020**, *16*, e2000955; b) S. Kusama, T. Saito, H. Hashiba, A. Sakai, S. Yotsuhashi, *ACS Catalysis* **2017**, *7*, 8382-8385.

[111] T. He, K. Reuter, A. Du, *Journal of Materials Chemistry A* **2020**, *8*, 599-606.

Table of Content

This review summarizes the recent work on the synthesis of carbon-supported SACs and their application in electrochemical CO_2 reduction to produce CO and other C_1 and C_2 products. Several different types of carbon-supported SACs are involved, including MN_x catalysts, heterogeneous molecular catalysts and the COFs based single atoms.

Keywords: carbon-supported single-atom, electrocatalyst, CO_2 reduction, metal-substrate intercalation.

Yuanzhi Zhu,[1] Xiaoxuan Yang,[1] Cheng Peng, Cameron Priest, Yi Mei, and Gang Wu**

Carbon-supported Single Metal Site Catalysts for Electrochemical CO_2 Reduction to CO and Beyond

ToC figure